Journal of CO2 Utilization 88 (2024) 102948

Contents lists available at ScienceDirect

Journal of CO2 Utilization

journal homepage: www.elsevier.com/locate/jcou

Low-carbon high-strength engineered geopolymer composites (HS-EGC) with full-volume fly ash precursor: Role of silica modulus

Ling-Yu Xu [a,b], Jian-Cong Lao [c], Lan-Ping Qian [b,d,*], Mehran Khan [e], Tian-Yu Xie [f], Bo-Tao Huang [a,b,**]

[a] Institute of Advanced Engineering Structures, Zhejiang University, Hangzhou, China
[b] Department of Civil and Environmental Engineering, The Hong Kong Polytechnic University, Hong Kong, China
[c] Department of Civil Engineering, The University of Hong Kong, Hong Kong, China
[d] Faculty of Urban Construction, Beijing University of Technology, Beijing, China
[e] School of Civil Engineering, University College Dublin, Dublin, Ireland
[f] School of Civil Engineering, Southeast University, Nanjing, China

ARTICLE INFO

Keywords:
Engineered Geopolymer Composites (EGC)
Strain-Hardening Geopolymer Composites (SHGC)
Alkali-Activated Materials (AAM)
Fly Ash
Silica Modulus
Over-Saturated Cracking

ABSTRACT

In this study, the influence of the silica modulus of alkaline activators on the overall performances of pure fly ash (FA)-based High-Strength Engineered/Strain-Hardening Geopolymer Composites (HS-EGC/SHGC) was comprehensively studied. The developed HS-EGC successfully presented simultaneous high compressive strength (over 90 MPa) and high tensile ductility (over 6.0 %) for the first time. Tensile strain-hardening and over-saturated cracking phenomena were observed for all the HS-EGC mixes. It was found that the increase of the silica modulus from 1.0 to 2.0 reduced the tensile strength and strain energy density of HS-EGC, but the most distinguished overall mechanical index was achieved in the mix with the silica modulus of 1.5. Additionally, the underlying mechanism behind the mechanical performances was explored by Back Scattering Electron and Energy Dispersive Spectroscopy (BSE-EDS) tests. According to the data comparison from literature review, the good sustainability and market potential of the developed material were successfully demonstrated, and the developed HS-EGC pushed the performance envelope of pure FA-based EGC materials. The findings could help promote the future development and practical applications of this strain-hardening geopolymer material with both good sustainability and high mechanical performances.

1. Introduction

As a modern high-performance construction material, Engineered Cementitious Composites (ECC) [also usually termed as Strain-Hardening Cementitious Composites (SHCC)] are well-known for its excellent tensile ductility (typically over 3 %), which is usually several hundred times that of the ordinary concrete [1–5]. Although conventional concrete is still the most widely adopted construction material [6–12], smart construction materials have become more popular for resilient infrastructure [13–16], and increasing attentions have paid to ECC technologies in recent years. By combining the matrix particle packing technology of ultra-high-performance concrete (UHPC) and the micromechanical design theory of ECC, high-strength ECC (HS-ECC) can be developed with a combined high compressive strength (> 80 MPa) and excellent tensile ductility (> 3 %) [17–19]. The above high-performance concrete material has a great potential for modern construction in the world, but still shows non-negligible drawbacks of high carbon footprint due to the inevitable high consumption of Portland cement [20,21]. Although supplementary cementitious materials can be adopted to partially replace Portland cement in cement-based materials [22], the sustainability issue is still a vital problem remains to be solved [23,24]. To address this challenge, the clinker-free geopolymer can be a promising substitution for the binding system of the above construction materials [25].

Free from hydration process and Ca-based C-S-H gel formation, geopolymers gain their strength from three-dimensional cross-linked N-

* Corresponding author.
** Corresponding author at: Institute of Advanced Engineering Structures, Zhejiang University, Hangzhou, China.
E-mail addresses: ling-yu.xu@connect.polyu.hk (L.-Y. Xu), Attic.lao@connect.polyu.hk (J.-C. Lao), lanping.qian@connect.polyu.hk (L.-P. Qian), Drmehrankhan@outlook.com (M. Khan), tianyuxie@seu.edu.cn (T.-Y. Xie), botaohuang@zju.edu.cn (B.-T. Huang).

https://doi.org/10.1016/j.jcou.2024.102948
Received 16 June 2024; Received in revised form 29 July 2024; Accepted 28 September 2024
Available online 4 October 2024
2212-9820/© 2024 The Author(s). Published by Elsevier Ltd. This is an open access article under the CC BY license (http://creativecommons.org/licenses/by/4.0/).

A-S-H gels after their hardening process [26–28]. Therefore, the precursors of geopolymers should be reactive aluminosilicate materials, and many types of industrial wastes [e.g., coal fly ash (FA)] can be potential sources [29,30], guaranteeing geopolymer productions able to show additional values apart from waste disposal [31–34]. Compared to cement-based concrete, clinker-free geopolymer concrete can achieve similar or even better mechanical characteristics and durable performances, but 50–80 % less carbon dioxide emissions [20,21,35,36]. In recent years, through replacing the cement clinkers of ECC with geopolymer binders, sustainable Engineered Geopolymer Composites (EGC) with low carbon footprint have been developed [25,37,38]. Similar to cement-based ECC, the tensile performance of EGC also follows the micromechanical design theory, which can show distinguished tensile strain-hardening and multiple cracking behaviors [39,40]. Through proper mix design of the geopolymer matrix as well as the fiber/matrix interface bonding, several breakthroughs have been made in the index of the tensile ductility of EGC, which has reached 13.7 % and 22 % as reported by Nguyễn et al. in 2021 [41] and Lương et al. in 2023 [42], respectively. On the other hand, by adopting highly reactive precursors with different particle sizes, high-strength geopolymer matrix can be developed guided by the particle packing theory. It is mentioned here that in recent years, Lao et al. [43] has successfully developed high-strength EGC (HS-EGC) whose compressive strength ranged from 94.4 MPa to 180.7 MPa with the corresponding tensile ductility located within 8.1–9.9 %, using FA, ground granulated blast furnace slag (GGBS) and silica fume (SF) as raw precursors. The findings of the referred work demonstrated the feasibility of developing EGC with both excellent compressive and tensile characteristics.

From current strengthening technologies of geopolymers, the assistance of highly amorphous Ca-rich GGBS looks essential for the development of HS-EGC [43]. Unlike three-dimensional cross-linked N-A-S-H gels sourced from aluminosilicate phases, alkali-activated GGBS gains strength from chain-structured C-A-S-H gels [44], which normally presents features of quick hardening and high hardened compressive strength at ambient temperature [45]. Therefore, GGBS is an effective raw material to improve the mechanical properties of FA-based geopolymers. Recently, Lao et al. [46] developed fly ash-dominated HS-EGC with a compressive strength over 120 MPa and a tensile ductility of 8 %, by introducing 19 % GGBS and 5 % SF by binder weights. Pan et al. [47] also produced HS-EGC with compressive strengths over 80 MPa through hybridization of GGBS and FA precursors, and examined their dynamic compressive responses. However, such blended geopolymer system may have some shortcomings, such as higher shrinkage [48] and lower fire resistance [49]. In addition, as GGBS shows a higher market price than FA, the replacement of FA by GGBS in geopolymer systems would inevitably increase the overall material cost. The addition of GGBS will also highly shorten the setting time of FA-based geopolymers, which is not beneficial for the in-situ construction of engineering structures [50]. Considering that no publications have been reported on HS-EGC developed with pure fly ash, it is essential to make some efforts to overcome this barrier. Furthermore, according to the knowledge of geopolymer science, different silica moduli (i.e., molar ratio of SiO_2/-Na_2O) of the alkaline activators can provide different contents of free silicate ions, which will highly change the molecular structures of N-A-S-H gels [51]. However, so far, there is also no published work that reported the influence of the silica modulus on the strain-hardening performances of HS-EGC, and scientific research is required to fill in this gap.

In this study, efforts were tried to develop HS-EGC with pure FA as the raw precursor, and the influence of silica moduli on the HS-EGC performance was investigated. Compressive and direct tensile tests were conducted to evaluate the mechanical properties of HS-EGC, and the crack evolutions of HS-EGC were assessed. Back Scattered Electron (BSE) with Energy Dispersive Spectroscopy (EDS) tests were conducted to investigate the microstructures and reaction products of the HS-EGC matrices. Also, an environmental assessment of the developed HS-EGC was performed. The investigation results aim to provide new insights and fulfill some gaps in the research field of fiber-reinforced geopolymer composites.

2. Experimental programs

2.1. Raw materials

Class F FA was used as the pure precursor in this study. According to X-ray fluorescence (XRF) tests and Scanning Electron Microscope (SEM) tests, its chemical compositions and morphologies are listed in Table 1 and presented in Fig. 1, where sphere-shaped FA particles with few irregular impurities were clearly observed. Fine silica sand (FSS) adopted as fine aggregates showed an averaged particle size smaller than 300 μm, a water absorption of 0.8 % and a specific gravity tested of 2.67 according to GB/T 14684–2011 [52].

Industrial-graded anhydrous sodium metasilicate (Na_2SiO_3-Anhydrous) particles (with 50.75 % Na_2O, 46.52 % SiO_2 and 2.73 % impurities) and waterglass (with 27.7 % SiO_2, 8.7 % Na_2O and 56.8 % H_2O) were both adopted as alkaline activators. Their silica moduli (molar ratios of SiO_2/Na_2O) were calculated as 0.94 and 3.18, respectively. Ultra-high-molecular-weight polyethylene (PE) fibers, which can easily favor high fiber-bridging forces and are normally adopted in HS-ECC/EGC materials, were used to reinforce HS-EGC specimens in this work. Their material characteristics are presented in Table 2.

2.2. Preparations of FA-based HS-EGC

This study aims to explore the influence of the silica modulus of alkaline activators on the macroscopic characteristics and microstructures of HS-EGC. Thus, three different silica moduli (i.e., 1.0, 1.5 and 2.0) were adopted while the alkalinities of alkaline activators (mass ratios of Na_2O to precursors) in different mixes were kept the same at 6 % through adjusting the mix proportions of Na_2SiO_3-Anhydrous and waterglass. The mix proportions of the three groups of HS-EGC are listed in Table 3. The mix ID "Gm" represents the HS-EGC mix produced by the alkaline activator with a silica modulus of "m".

Prior to the formal casting of HS-EGC, the alkaline activators should be prepared first. Na_2SiO_3-Anhydrous, waterglass and extra water were mixed (Table 3) and stirred to form uniform alkaline solutions, and the solutions were then cooled down to the environmental temperature. Next, solid matrix source materials including FA and FSS were dry-mixed for 3 min with a low rotating speed, after which the prepared alkaline solution was added into the mixer and a consequent stirring of 10 min was conducted. After the fresh paste became uniform, PE fibers were slowly dispersed into the mixer, and a further stirring of 5 min was conducted. Afterwards, the flowability of fresh mixtures were subsequently tested, according to ASTM C1437 [53]. The mini-slump spread diameters of G1.0, G1.5, and G2.0 were measured as 131 mm, 136 mm, and 140 mm, respectively. It indicates that the increase of the silica modulus of the activator could result in an improvement of the flowability of HS-EGC. After the measurement, HS-EGC was cast into the prepared molds. After a hardening process of 24 h, the specimens were carefully demolded, sealed, and heat-cured under the 90 °C condition for 72 h. Finally, the specimens were sealed under room temperature until formal tests.

2.3. Testing methods

Both compressive and direct tensile tests were conducted to evaluate the mechanical performances of HS-EGC. Three 50-mm-diameter cubic specimens were prepared for compressive tests [54]. The compressive test was conducted under a universal compression machine, and the loading rate was set as 1.0 MPa/s. On the other hand, three dumbbell specimens (Fig. 2) were tested under the displacement rate of 0.5 mm/min using a 50 kN-tension machine [55]. The elongation of the

Table 1
Chemical components of fly ash (%).

Chemical Composition	Al_2O_3	SiO_2	CaO	Fe_2O_3	MgO	SO_3	TiO_2	P_2O_5	K_2O	Others	LOI
FA	21.92	45.24	8.59	12.60	4.74	1.56	1.55	0.64	1.69	0.66	1.47

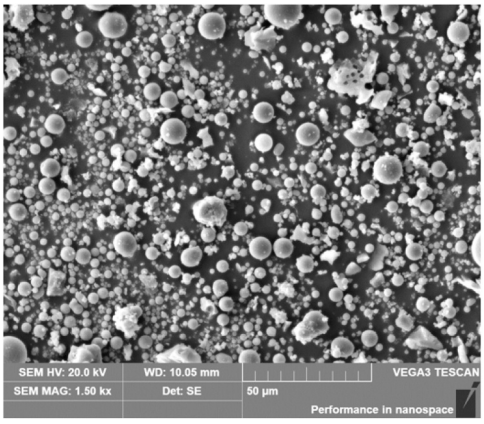

Fig. 1. Morphology of FA particles observed from SEM test.

specimens (a section area with an 80-mm gauge length) was measured by two linear variable differential transformers (LVDTs), which were fixed along two lateral sides of the dumbbell specimens, and a high-resolution camera was used to record the entire deformation and cracking process of HS-EGC at an interval of 3 s. ImageJ software was used to evaluate the cracking patterns of HS-EGC from the recorded photographs.

After the mechanical tests, the analyses of microstructures and reaction products of HS-EGC fragments were conducted. The fragments were taken from dumbbell specimens, fixed by hardened resins, and freeze-dried at −80 °C for 4 h. During the BSE tests, the samples were vacuumed, and observed under 1000× magnifications. EDS point measurements (around 45 points) were performed on the reacted gel regions [43].

3. Tensile properties and strain-hardening behavior

3.1. Tensile stress-strain curves

The tensile stress-strain curves of the HS-EGC dumbbell specimens with different silica moduli and the averaged ones are presented in Fig. 3. Significant strain-hardening behaviors and double-stage evolutions of tensile stress–strain curves were observed in all three HS-EGC types. To better compare their tensile performances, the corresponding tensile properties (i.e., tensile strength, cracking strength, tensile strain capacity, averaged crack width at the ultimate stage, and strain energy density) are recorded in Table 4 and Fig. 4.

The tensile performance of fiber-reinforced cementitious/geopolymer materials is guided by the micromechanical design principles [56,57]. Among the three mixes, G1.0 showed the highest tensile cracking strength (9.2 MPa) and the tensile strength (13.9 MPa). As the silica modulus increased from 1.0 to 2.0, both the two indices showed decreasing trends, where G1.5 had a tensile cracking strength of 6.7 MPa and a tensile strength of 12.8 MPa, while the two indices of G2.0 were 5.9 MPa and 10.7 MPa, respectively. This finding is almost in accordance with that obtained by Zhang et al. [58]. As the ultimate tensile strength of HS-EGC is directly related to the fiber/matrix interfacial bond, the above finding also indicated that a lower silica modulus (lower than 2.0) is beneficial for improving the fiber/matrix bond properties. However, as the tensile cracking strength also increased with the decrease of the silica modulus, the highest tensile strain capacity was not achieved in G1.0 (6.0 %), but in G1.5 (6.7 %). In comparison, G2.0 also showed higher tensile strain capacity (6.5 %) than G1.0, due to the lower tensile cracking strength of the former mix (5.9 MPa). The tensile strain capacity also seems to show a similar trend with the ratio of tensile strength to cracking strength of HS-EGC, as presented in Fig. 5. This finding demonstrated that a lower cracking strength as well as a stronger fiber/matrix bond is advantageous to the tensile strain-hardening behaviors of EGC materials. Additionally, the strain energy densities (represented by the area under the tensile stress-strain curves before the ultimate failure stage) were also calculated and presented in Fig. 4**e**. Among the three mixes, G1.0 had the highest strain energy density (650.3 kJ/m^3), and the value of this index decreased with the increase of silica modulus. Remarkably, inflection points can be observed in the stress-strain curves of all the mixes under direct tension (Fig. 3), and the curve slopes significantly increased after the inflection. These phenomena were related to the over-saturated cracking of

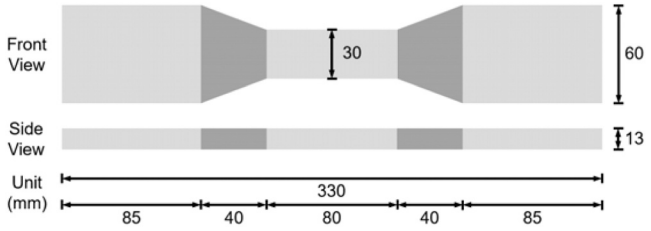

Fig. 2. Geometry of the dumbbell specimens of HS-EGC.

Table 2
Material characteristics of PE fibers.

PE Fibers	Strength (MPa)	Modulus (GPa)	Length (mm)	Diameter (μm)	Density (g/cm^3)
Basic Properties	3000	100	18	24	0.97

Table 3
Mix proportions of HS-EGC (weight ratio).

Mix IDs	Precursors	Alkaline Activators			Extra Water	Total Water	FSS	PE Fibers
	FA	Na_2SiO_3-Anhydrous	Waterglass (56.8 % water)	Silica modulus				
G1.0	1.000	0.116	0.016	1.0	0.171	0.180	0.300	2.0
G1.5		0.090	0.162	1.5	0.088			(vol%)
G2.0		0.065	0.310	2.0	0.004			

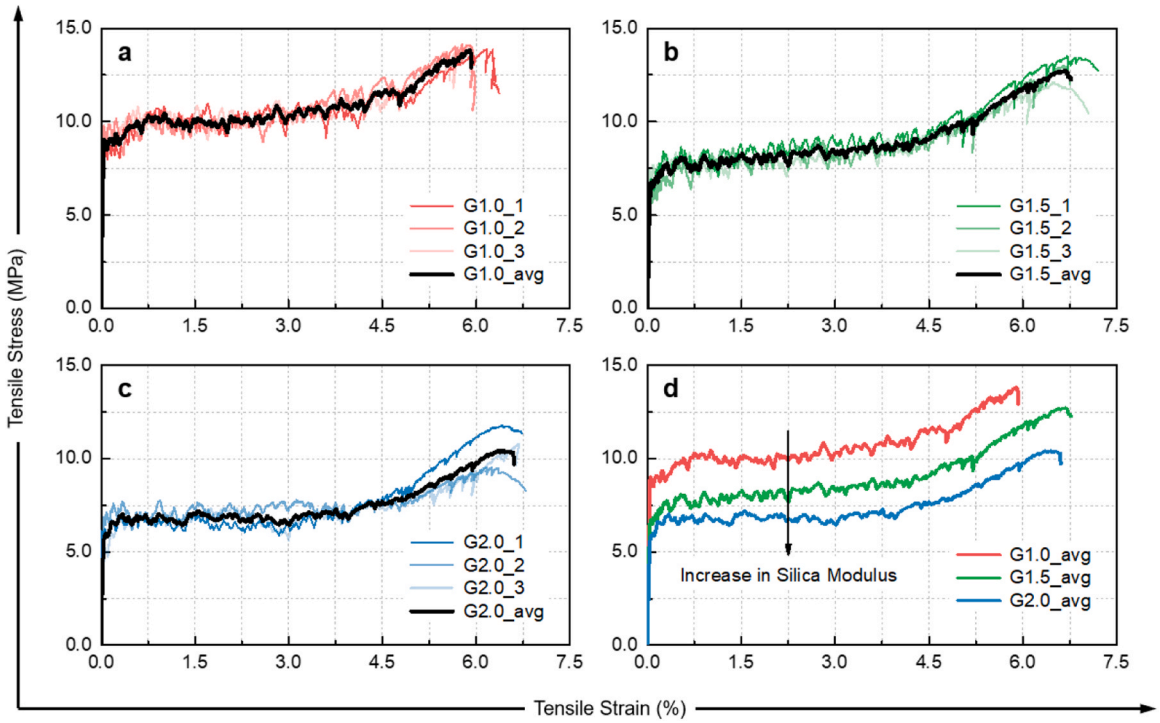

Fig. 3. Tensile stress-strain curves of HS-EGC with different silica moduli: (a) G1.0, (b) G1.5, (c) G2.0, and (d) comparison of averaged curves. Double-stage evolutions of tensile stress–strain curves were observed in all the mixes.

Table 4
Mechanical properties of HS-EGC.

Mechanical Properties	G1.0	G1.5	G2.0
Compressive Strength, f'_c (MPa)	89.9 ± 1.0	93.0 ± 7.4	73.5 ± 2.6
Tensile Strain Capacity, ε_t (%)	6.0 ± 0.2	6.7 ± 0.2	6.5 ± 0.2
Ultimate Tensile Strength, f_t (MPa)	13.9 ± 0.4	12.8 ± 0.7	10.7 ± 1.2
Tensile Cracking Strength, f_{to} (MPa)	9.2 ± 0.6	6.7 ± 0.8	5.9 ± 1.2
Average Crack Width at the Ultimate Strain, w_u (μm)	73.0 ± 12.8	71.6 ± 2.9	58.4 ± 9.3
Strain Energy Density, u (kJ/m^3)	650.3 ± 22.7	608.3 ± 47.0	484.9 ± 13.1
$f'_c f_t \varepsilon_t / w_u$ Index (MPa^2/μm)	1.01	1.11	0.88

HS-EGC [59], and the detailed analyses would be presented in **Section 3.3** and **Section 3.4**.

3.2. Crack width at the ultimate stage

The crack width is an important parameter for the durability of cement/geopolymer-based construction materials [60–64]. The averaged crack widths at the ultimate stages were obtained from digital photos using ImageJ software, and the results are presented in Fig. 4**d** and Table 4. The cracking patterns of different EGC mixes are also presented in Fig. 6 to make a clear observation. Obviously, the averaged crack width decreased with the increase of silica modulus, where G1.0, G1.5 and G2.0 had averaged crack widths of 73.0 μm, 71.6 μm, and 58.4 μm, respectively. This result is also in accordance with the observations in Fig. 6 and the fluctuations of stress drops in the tensile stress-strain curves (larger fluctuations indicate the occurrence of cracks with larger widths [65]), where G2.0 showed the smoothest tensile stress-strain curves. Therefore, although higher silica modulus may not

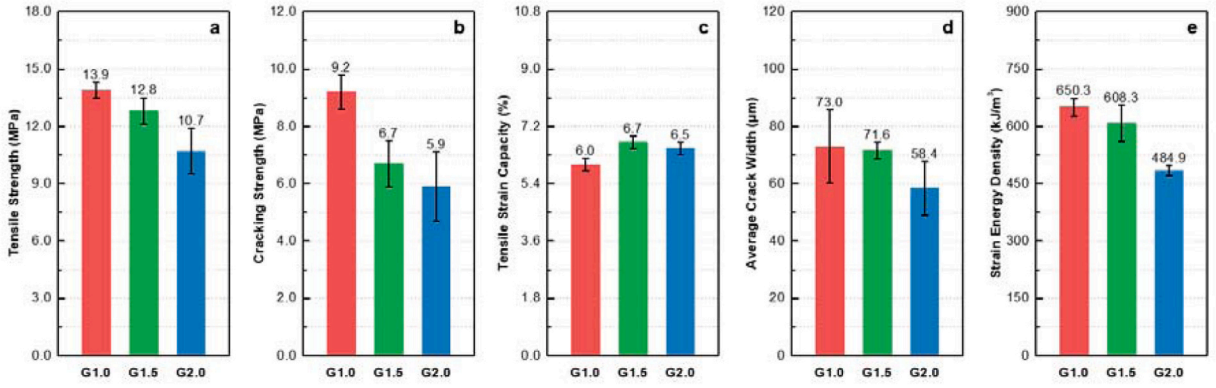

Fig. 4. Tensile performances of HS-EGC with different silica moduli (a) Tensile strength, (b) cracking strength, (c) tensile strain capacity, (d) averaged crack width at the ultimate stage, and (e) strain energy density.

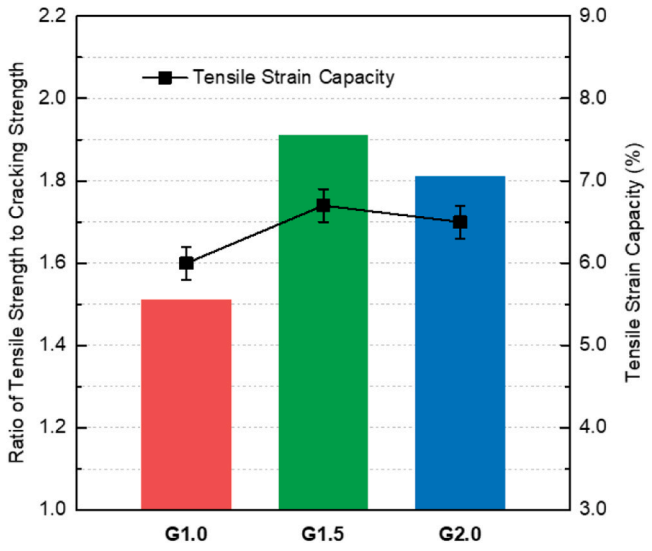

Fig. 5. Tensile strain capacities and ratios of tensile strength to cracking strength of different EGC mixes. G1.5 showed the highest tensile strain capacity and the highest value of the ratio of tensile strength to cracking strength.

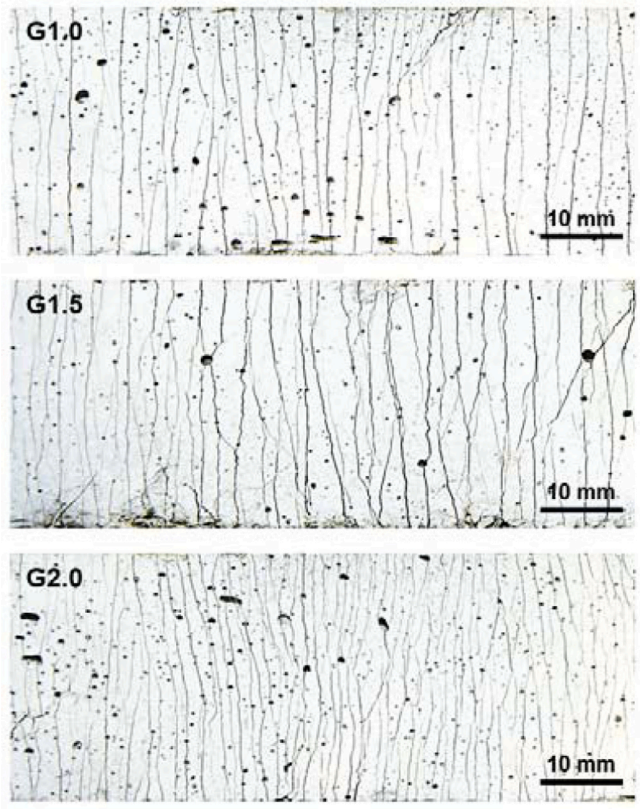

Fig. 6. Crack patterns of HS-EGC at the ultimate tensile strain. Fine cracks were evenly distributed for all the mixes and G2.0 showed the finest crack width.

be positive to enhance certain tensile properties (e.g., tensile strength and strain energy density), it is beneficial for reducing the crack width of HS-EGC and improving their durability properties.

3.3. Double-stage crack evolution

As mentioned in **Section 3.1**, obvious inflection points can be observed in Fig. 3. Because the deformation properties of HS-EGC are directly associated with its crack number and averaged crack width, the occurrence of the deflection points could be determined by the crack evolution conditions. Therefore, the crack numbers and averaged crack width at different strain levels (i.e., 0.5 %, 1.0 %, 1.5 %, …, the ultimate strain) were calculated from digital photos with the assistance of ImageJ software, and the results are presented in Fig. 7, respectively. It is noted that the first sample of each mix (i.e., G1.0_1, G1.5_1, and G2.0_1 in Fig. 3) was adopted for the crack analysis. From Fig. 7, it can be observed that the crack number evolution shows a double-stage pattern, which is in accordance with the slope changes of the tensile stress-strain curves. At the first stage, the crack number showed a steady and fast increasing trend, while after the inflection point, the crack number increase rate obviously decreased. From the averaged crack width evolution curves (Fig. 7), a similar inflection point could be observed, which also divided the crack width evolution curves into two stages. At the first stage, the crack evolution pattern showed a constant crack width or slow crack opening, which is the same with the steady-state cracking of ordinary ECC materials [66]. However, at the second stage, a distinguished slope increase was observed in the crack width evolution curves of all the three mixes, indicating that crack opening dominated at this stage. Interestingly, compared to the inflection points of the tensile stress-strain curves, crack number evolution curves and the averaged crack width evolution curves were almost overlapped (approximately 4.5 % for G1.0, 4.0 % for G1.5, and 4.0 % for G2.0), indicating the close relationship among these three characteristics. As summarized by Xu et al. from their studies on HS-ECC [59], the second stage showed slow crack number increase and significant crack opening, and its mechanism will be discussed in **Section 3.4**.

3.4. Over-saturated cracking mechanism

The mechanism of tensile over-saturated cracking of cementitious/geopolymer materials with strain-hardening properties is summarized in Fig. 8 [59]. In the figure, σ_{fc} and ε_{fc} represent the tensile cracking strength and its corresponding strain, σ_{1xd} and ε_{1xd} represent the stress and strain corresponding to the theoretical cracking limit x_d, σ_{2xd} and ε_{2xd} represent the stress and strain corresponding to the doubled theoretical cracking limit $2x_d$ (usually regarded as a threshold between saturated cracking condition and unsaturated cracking condition according to micromechanical theory [67]), and x_d^t represent the crack spacing tested at the ultimate stage during the experimental test. Both low matrix fracture toughness and strong fiber-bridging force are beneficial for inducing over-saturated cracking phenomena.

In this study, tensile over-saturated cracking phenomenon was found in all the three mixes, possibly due to the comparatively low fracture toughness of FA-based geopolymer matrix and high bridging force between PE fibers and the geopolymer matrix. At the first stage, the conventional steady-state multiple crack evolution dominated with a stable crack number increase but slow crack opening. For normal ECC/EGC, this stage usually finishes before the strain reached ε_{1xd}, which represented the end of the saturated cracking stage. However, for HS-EGC developed in this study, the second stage occurred with no significant crack number increase but distinguished crack opening, which further enhanced the strain-hardening characteristics of HS-EGC. More detailed definition and illustration of over-saturated cracking phenomenon could be seen in Ref. [59]. In fact, realizing the over-saturated cracking behavior is helpful for the full utilization of HS-EGC with both excellent strength indices and tensile strain capacity: On one hand, the first stage with narrowed and stable crack width is preferrable for long-term durability of infrastructure under normal practical service. On the other hand, the second stage with improved hardening characteristics can be helpful to strengthening the resilience of infrastructure under extreme loading conditions, where the crack opening control is of less significance but the ultimate deformability plays a more important role. It is mentioned here that compared to cement-based HS-ECC, tensile over-saturated cracking behavior was more easily achieved in HS-EGC

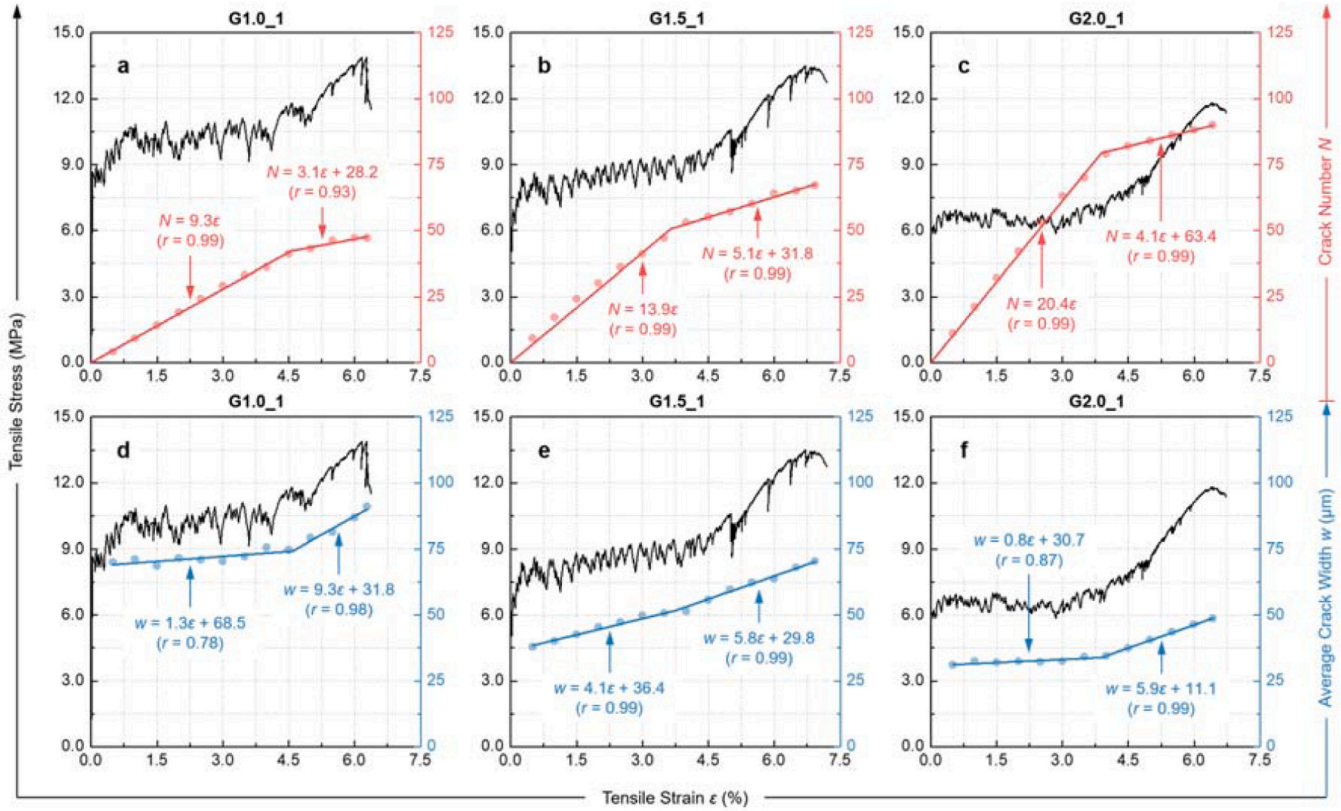

Fig. 7. Cracking behavior of HS-EGC at different strain levels: Crack numbers [(a) G1.0, (b) G1.5, and (c) G2.0] and averaged crack widths [(d) G1.0, (e) G1.5, and (f) G2.0]. Double-stage evolutions of crack numbers and average crack widths were observed for all the mixes.

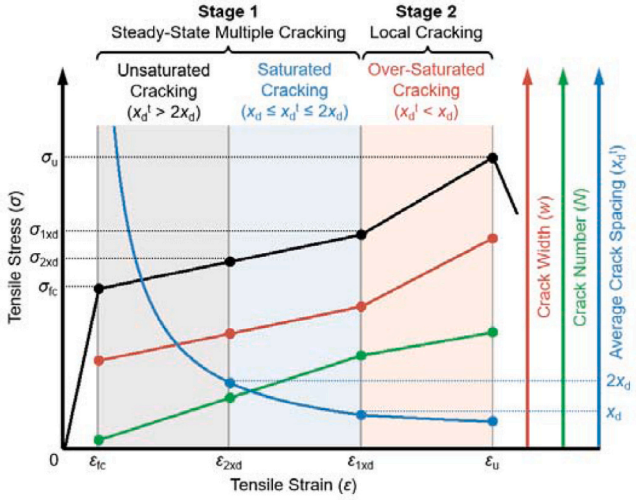

Fig. 8. Schematic diagram of tensile over-saturated cracking of strain-hardening cementitious/geopolymer composites [59].

with low fracture toughness and high fiber-bridging strength. The over-saturated cracking stage can be utilized to improve the resilience of HS-EGC structural members under extreme loading conditions (e.g., seismic and impact loadings).

4. Compressive properties, microstructures, and elemental analyses

4.1. Compressive strength

The compressive strengths of HS-EGC with different silica modulus are presented in Table 4 and Fig. 9. The highest compressive strength was achieved in G1.5 (93.0 MPa), the middle one was obtained in G1.0

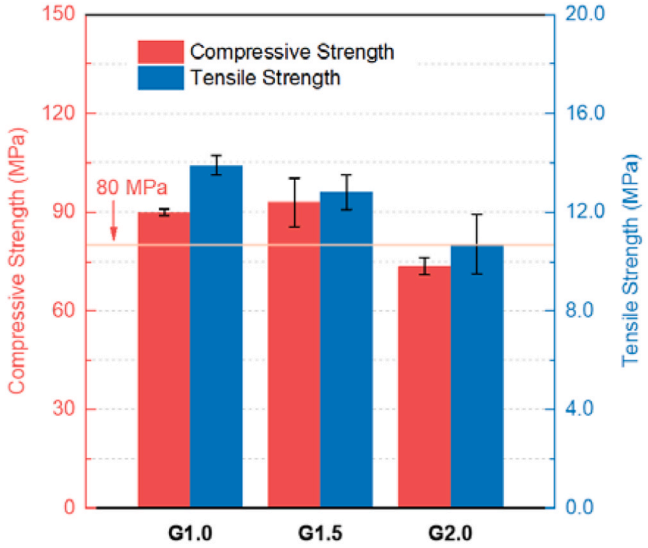

Fig. 9. Compressive and tensile strengths of HS-EGC with different silica moduli. When the silica modulus increased to 2.0, the deterioration of strength was observed.

(89.9 MPa), while the lowest one was observed in G2.0 (73.5 MPa), which are in accordance with the previous results obtained by Ouyang et al. [68]. Therefore, G1.0 and G1.5 can be strictly classified as HS-EGC according to the definition of the analogue HS-ECC (with a compressive strength over 80 MPa) [18]. The reaction degree of geopolymer pastes is highly associated with soluble Si monomers as well as the pH values of the solution environments. When silica moduli of activators increased from 1.0 to 1.5, more silicate species are provided in the activator solution, resulting in an increase of N-(C)-A-S-H gel volume which allows for a higher strength [69]. However, when the silica modulus further increased to 2.0, deterioration of strength was observed, possibly due to the excessive reduction of pH value of the activator solution as the silica modulus increased. As depicted by Chang [70], with Na_2O content fixed, the increase of SiO_2/Na_2O would induce a reduction of pH values of the solution. Furthermore, the excessive silicate in the solution could reduce the Al content in the reaction product, and thus deteriorate the strength (will be discussed in **Section 4.3**). Therefore, a silica modulus of alkaline activators over 2.0 is not beneficial for the full pozzolanic reaction of geopolymers and will hinder its strength development [71].

4.2. BSE morphology

Fig. 10 displays the BSE images of HS-EGC matrices with different silica moduli. In the figures, the spherical light particles were unreacted FA particles, the grey regions were the formed N-(C)-A-S-H gels, and the round dark holes were the pores left after FA dissolution or some possible initial flaws [40,46]. As can be seen from the figure, G1.5 showed the densest microstructures with the least unreacted FA particles, indicating the high degree of reaction in this mix. In comparison, G1.0 had a comparatively dense microstructure coinciding well with its high strength, which was only slightly lower than that of G1.5. However, G1.0 still possessed a large amount of unreacted FA particles, which had a high elastic modulus and could contribute to a high tensile strength [43]. When the silica modulus reached 2.0, the alkali-activation reaction was slower due to the relatively lower pH value of the activators as aforementioned, and more macro pores were observed, which could be the reason for the lowered mechanical performance of geopolymers of this mix. This phenomenon is also in accordance with the previous finding reported by De Vargas et al. [72]. As macro pores could work as flaws in geopolymer matrix which can facilitate new crack formation, G2.0 with more macro pores thus showed a more distinguished over-saturated cracking phenomenon (i.e., the second stage as presented in Fig. 3**c**). Moreover, several microcracks could be observed in the three mixes, which were mainly caused by geopolymer shrinkage or vacuum pumping under BSE observation [2]. As the generation of microcracks could also to some extent indicate the toughness of the matrix, G1.5 obviously presented the best mechanical performance, while G2.0 had the highest crack resistance properties, which are in agreement with the macroscopic mechanical characteristics as reported in previous sections.

4.3. EDS analysis

EDS is an effective tool to evaluate the chemical assemblage of reaction products [73,74]. According to the EDS point measurements of the geopolymer gel phases, the obtained $(CaO+Na_2O)$-Al_2O_3-SiO_2 ternary phase diagrams of the HS-EGC gels are presented in Fig. 11, where the sum of the normalized $(CaO+Na_2O)$, SiO_2 and Al_2O_3 contents is 100 % by atomic ratio. The points were concentrated in the ternary phase diagrams, which represented N-(C)-A-S-H and indicated the validity of the test. The N-(C)-A-S-H network consisted of SiO_4 tetrahedra and AlO_4^- tetrahedra units, where cations are necessary to balance the negative charge from AlO_4^- tetrahedra [43]. Thus, the Al/Si and (Ca + Na)/Si ratios could reflect the change of N-(C)-A-S-H.

To further analyze the compositions of N-(C)-A-S-H, statistical analyses of Al/Si ratios and (Ca+Na)/Si ratios were performed on the three HS-EGC mixes, and the relevant results are shown in Fig. 12 and Fig. 13. The data distribution and the mean values of Al/Si ratios and (Ca+Na)/Si ratios were fitted by Gaussian distribution, which are also marked in the figures as the representative parameter for each mix.

Interestingly, the Al/Si ratios of G1.0 and G2.0 were similar (0.36 for G1.0 and 0.34 for G2.0), but the value of G1.5 was much higher (0.46). The (Ca + Na)/Si ratios showed a similar trend, where the averaged values of G1.0 and G2.0 were both 0.12, while that of G1.5 was 0.15. The same trend of Al/Si and (Ca + Na)/Si resulted from the nature that both Na^+ and Ca^{2+} were necessary for the charge balance of AlO_4^- in N-(C)-A-S-H. As the water molecules were structurally presented in $Na^+(H_2O)_n$ in N-(C)-A-S-H [75], the increase of Na^+ could result in a higher bound water content, which indicated that the N-(C)-A-S-H in G1.5 with a higher Al/Si content might exhibit a stronger water binding ability and contribute to a higher strength. The higher Al and Ca contents in N-(C)-A-S-H of G1.5 could possibly be correlated with the higher reaction degree of FA in this mix than those in G1.0 and G2.0 as observed in BSE, because FA particles were the only source of Al and Ca among the raw materials. By contrast, FA in G1.0 and G2.0 exhibited relatively lower degrees of reaction due to the lower silicate content and lower pH in the activator solution, respectively, and thus provided less Al and Ca to form N-(C)-A-S-H gels.

5. Comparisons of mechanical performances, environmental impact, and economic efficiency with the results in existing literature

5.1. Assessment of overall performance

As different mechanical performances of HS-EGC did not strictly follow the same trend with the variations of silica modulus, it is of great

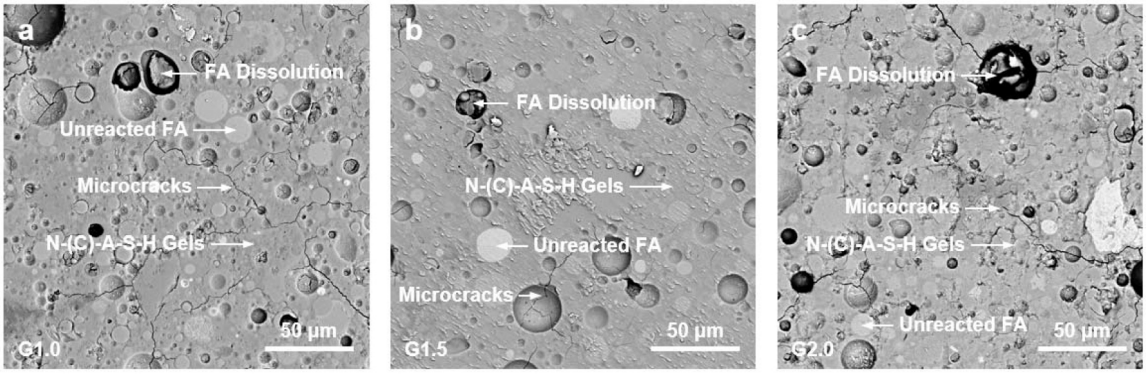

Fig. 10. BSE images of HS-EGC matrices with different silica moduli (a) G1.0, (b) G1.5, and (c) G2.0. Compared to G2.0, G1.0 and G1.5 showed denser microstructures.

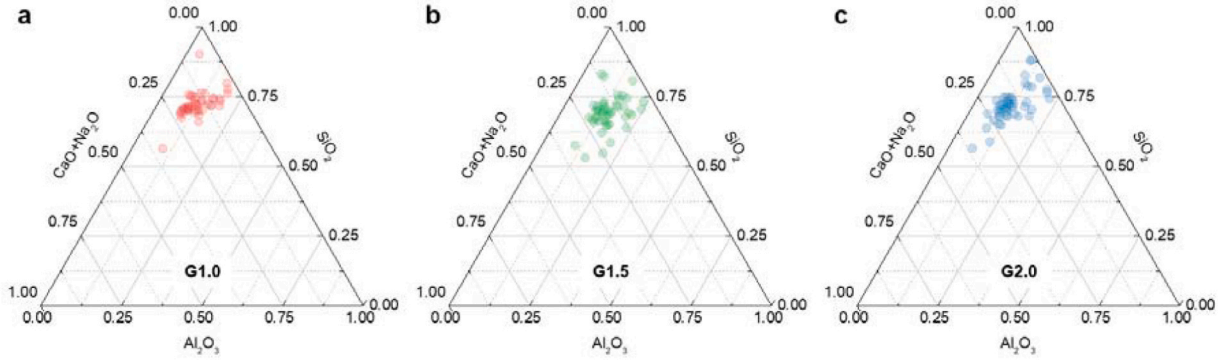

Fig. 11. (CaO+Na_2O)-Al_2O_3-SiO_2 ternary phase diagrams of the HS-EGC gels. The points were concentrated in the ternary phase diagrams, which represented N-(C)-A-S-H.

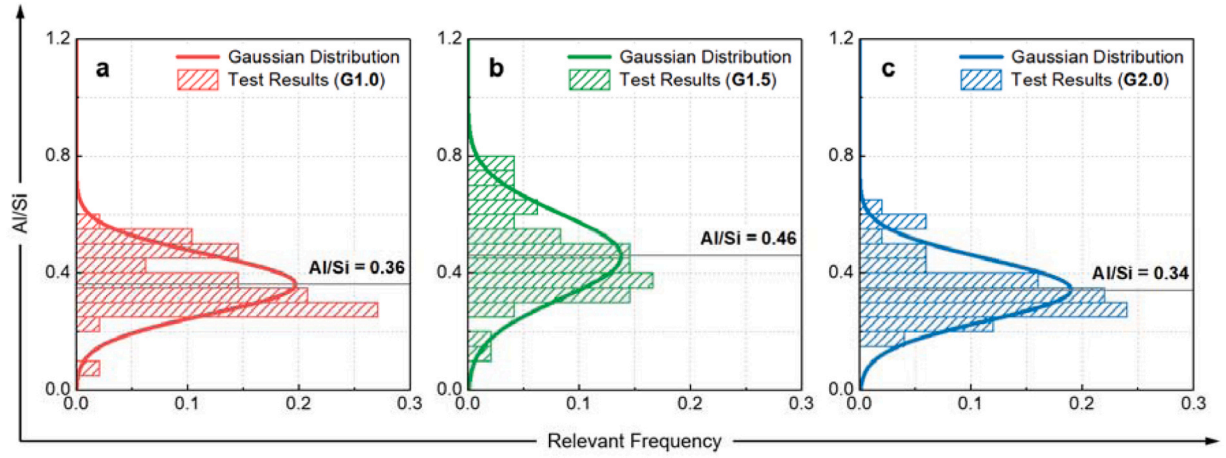

Fig. 12. Statistical analysis of the Al/Si ratios of HS-EGC gels (fitted by Gaussian Distribution): (a) G1.0, (b) G1.5 and (c) G2.0. G1.5 showed the highest Al/Si ratio.

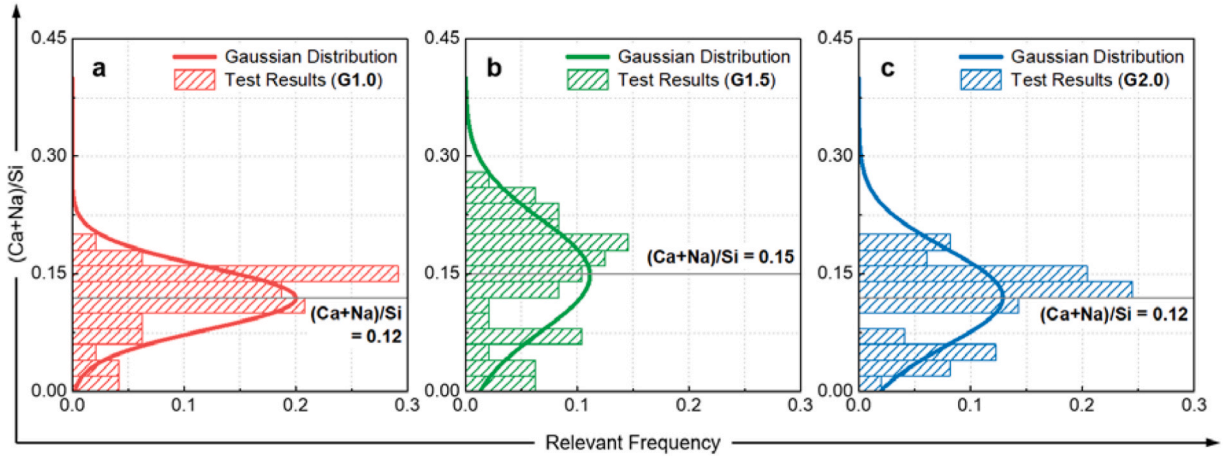

Fig. 13. Statistical analysis of the (Ca+Na)/Si ratios of HS-EGC gels (fitted by Gaussian Distribution): (a) G1.0, (b) G1.5 and (c) G2.0. G1.5 showed the highest (Ca+Na)/Si ratio.

significance to define a representative index to indicate the overall performances of HS-EGC. In this study, the overall index $f'_c f_t \varepsilon_t / w_u$ proposed by Huang et al. [76] was adopted to evaluate the overall performance of HS-EGC (as listed in Table 4), as different properties including compressive strength, tensile strength, tensile strain capacity and averaged crack width at the ultimate stage were all considered. Because a larger crack width is not advantageous to the durability of HS-EGC, its reciprocal was adopted in the overall $f'_c f_t \varepsilon_t / w_u$ index. As seen from Table 4, the highest overall $f'_c f_t \varepsilon_t / w_u$ index was achieved in G1.5 (1.11 $MPa^2/\mu m$), while G2.0 showed the lowest value (0.88 $MPa^2/\mu m$). Additionally, a four-dimensional overall assessment of HS-EGC was plotted in Fig. 14. Because the crack width is not a positive factor for HS-EGC performances, its reciprocal was used for the assessment. As can been seen from the figure, G1.0 showed good strength indices but large crack width, as well as small tensile strain capacity, while G2.0 almost presented the opposite results. In comparison, G1.5 had the best overall

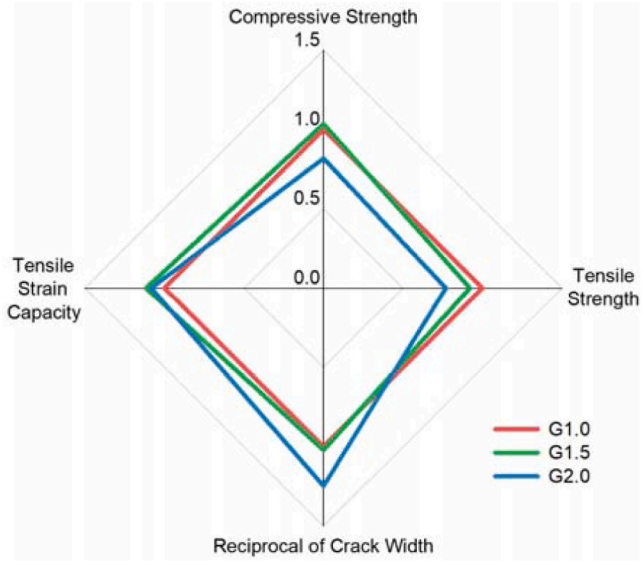

Fig. 14. Four-dimensional assessment of mechanical and cracking performances of HS-EGC. G1.5 showed the best overall performances.

mechanical and cracking performances. This finding is in accordance with the evaluation in terms of the overall $f'_c f_t \varepsilon_t / w_u$ index, indicating the best overall performance of the HS-EGC mix with a silica modulus of 1.5.

5.2. Comparisons of overall performances with FA-based EGC in existing literature

Apart from the sustainability issues, the mechanical performance could be regarded as the most important characteristic of construction materials. In this work, a comparison work was conducted for the compressive strengths and tensile strain capacities of HS-EGC materials (G1.0, G1.5, and G2.0) and the FA-based EGC materials from existing literature (Fig. 15), with the comparisons of their Strength-Ductility (SD) Indices are presented. Here, SD Index was the product of compressive strength and tensile strain capacity. In terms of SD Indices (Fig. 15**a**), the three mixes recorded much higher values (5.4, 6.2, and 4.8 MPa for G1.0, G1.5, and G2.0, respectively) than those of the currently available values, which were all below 3.0 MPa. It can also be observed in Fig. 15**b** that high compressive strength (around or over 90 MPa) and high tensile strain capacity (over 6 %) were not simultaneously achieved in previous work, but successfully realized in this study. In comparison, the developed HS-EGC in this work recorded the highest compressive strength values (G1.0 with 89.9 MPa and G1.5 with 93.0 MPa), and the second highest tensile strain capacity (The highest value was recorded by Nguyễn et al. [41] with a tensile strain capacity of 13.7 %), which showed much better overall mechanical performances than those from existing literature. Overall, the work in this study successfully pushed the performance envelope of pure FA-based EGC, which could help promote the future development and practical applications of this clinker-free strain-hardening geopolymer material with both high mechanical performances and good sustainability.

5.3. Environmental impact and economic efficiency

Apart from mechanical properties, the environmental impacts and economical efficiencies are both the critical factors for sustainable construction materials. Therefore, from the above two aspects, it is important and meaningful to assess the relevant characteristics of HS-EGC. To better evaluate the sustainability level of the developed HS-EGC, two types of strain-hardening cementitious materials, i.e., EGC materials developed with pure FA and cement-based HS-ECC with comparable compressive strengths from existing literature, were chosen as the comparisons.

As summarized from existing literature, the embodied carbon, embodied energy, and costs of different raw materials of ECC/EGC are

Table 5
Embodied carbon, embodied energy and costs of raw materials.

Raw Materials	Embodied Carbon [(kg CO_2)/kg]	Embodied Energy (MJ/kg)	Cost* (CNY/kg)
FA	0.004 [89]	0.100 [90]	0.298 [19]
Sodium Silicate	1.860 [27]	9.400 [91]	0.731 [19]
NaOH Anhydrous	0.625 [92]	10.800 [92]	2.73 [93]
Metakaolin (MK)	0.400 [94]	3.480 [94]	0.398 [94]
Lime Powder (LP)	0.017 [95]	0.350 [96]	0.321 [95]
Ground Granulated Blast-Furnace Slag (GGBS)	0.042 [89]	0.200 [91]	0.425 [19]
Sand	0.023 [97]	0.067 [97]	0.808 [19]
Water	0.001 [97]	0.100 [97]	0.006 [19]
Cement	0.912 [89]	5.500 [90]	0.680 [19]
Silica Fume (SF)	0.024 [98]	0.100 [90]	1.785 [19]
Superplasticizer (SP)	1.880 [89]	11.470 [90]	8.500 [90]
PVA Fiber	1.710 [99]	101.000 [99]	127.500 [99]
PE Fiber	2.000 [40]	94.500 [40]	170.000 [40]

* It is assumed that the HKD/CNY exchange rate is 0.85. For FA-based EGC in [84], 1.6 % MK was adopted as an additive.

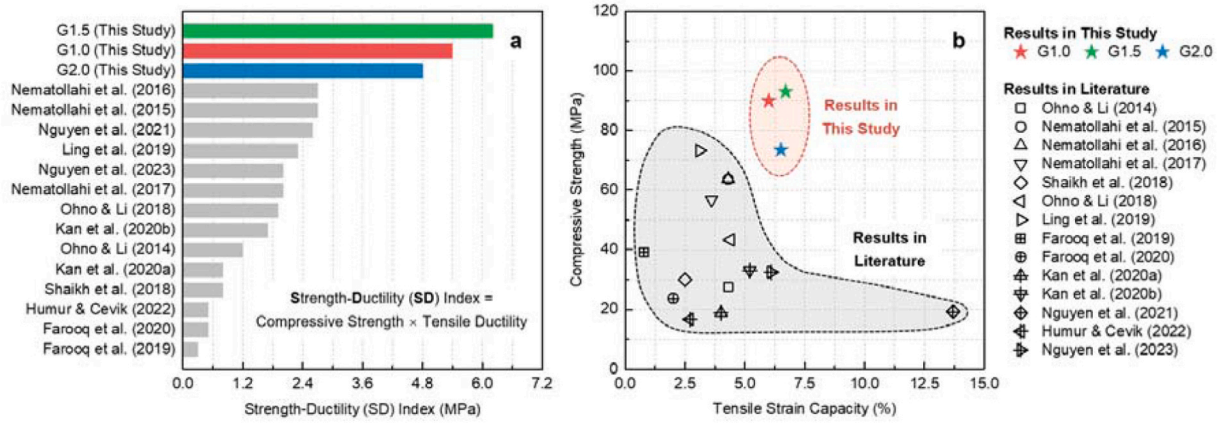

Fig. 15. Comparisons of the mechanical performances of the developed FA-based HS-EGC and existing FA-based EGC: (a) Strength-Ductility (SD) Index, and (b) compressive strength *vs.* tensile strain capacity relations [21,25,41,77–86]. The results in this study successfully pushed the performance envelope of pure FA-based EGC.

listed in Table 5. It should be noted that for some studies with unclear material dosages/types, the missing data were estimated based on those adopted in this study (e.g., the water content of waterglass). Also, as the components of waterglass were different in differed studies, this material was regarded as a combination of solid sodium silicate and free water during the calculation. Meanwhile, fine silica sand was assumed as the only sand type in all the cases, because this sand is the most commonly used in ECC/EGC materials. Moreover, to eliminate the influence of fiber contents on the mechanical performances of EGC/HS-ECC, mixes with 2 % fiber dosages (vol%) were selected as the targets if available. If no such fiber contents were adopted in referred studies, the mix with the best mechanical performances and the closest fiber dosages would be chosen for the comparison.

For the influence of heat curing, the generated energy consumption could be calculated by the following equation [87]:

$$Energy_{curing} = Pt_{curing} + mc(T_{curing} - 25) \quad (1)$$

where P represents the power of the chamber (600 W), t_{curing} represents the curing time, T_{curing} represents the curing temperature, m represents the mass, and c represents the specific heat capacity of the materials (assumed to be 700 J/kg/°C). During the heating process, the converted embodied carbon from energy consumption had an emission factor of 0.231 (kg CO_2)/kWh [88], and cost with local industrial electricity fee was 0.538 CNY/kWh in Hangzhou, China. Based on the mix proportions of different mixes and the above information, the embodied carbon, embodied energy, and material costs were calculated, and the results were listed in Table 6 together with corresponding mechanical properties. Additionally, to consider the coupled mechanical performance and sustainability issues, the strength-ductility (SD) indices were calculated by multiplying compressive strength and tensile strain capacity (i.e., $f'_c\varepsilon_t$) as recommended by Huang et al. [17], and the sustainability parameters per SD Index were also calculated and listed in the table.

5.3.1. Comparisons of embodied carbon

Embodied carbon is the sum of greenhouse gas emissions during the whole life cycle of materials, including raw material extraction, transportation, manufacturing, construction, and maintenance. The embodied carbon and embodied carbon per SD Index of HS-EGC, FA-based EGC and HS-ECC are presented in Fig. 16**a** and Fig. 16**b**, respectively.

For the HS-EGC developed in this study, sodium silicate and waterglass were the main contributors to embodied carbon. The higher silica modulus of activators was not beneficial to developing low-carbon HS-EGC, and the embodied carbon of HS-EGC increased from 375.1 kg CO_2/m^3 to 511.5 kg CO_2/m^3 as the silica modulus increased from 1.0 to 2.0. Comparing FA-based EGC, HS-ECC, and the HS-EGC developed in this study, HS-ECC obviously showed much higher embodied carbon (over 750.0 kg CO_2/m^3) due to the high dosages of the unsustainable Portland cement. In comparison, the HS-EGC developed in this study showed much lower carbon emission (375.1–511.5 kg CO_2/m^3) together with high compressive strengths, indicating the sustainable feature of clinker-free HS-EGC. Additionally, FA-based EGC from existing literature showed a similar range of embodied carbon with the HS-EGC developed in this study. From the figure, it could be observed that the main body of the carbon footprint was attributed to the alkaline activators (sodium silicate and NaOH), which is unavoidable for geopolymer materials at the current stage. The heat curing process did not contribute much to the carbon footprint of the HS-EGC development.

To compare the coupled mechanical and sustainable characteristics, the embodied carbon was divided by the SD Index, and the results are presented in Fig. 16**b**. Obviously, the HS-EGC developed in this study (especially G1.0) showed the lowest embodied carbon per SD Index in the FA-based EGC family due to its high compressive strength, high tensile ductility, and comparatively low total carbon emission, and the increasing silica modulus of alkaline activators also resulted in higher embodied carbon per SD Index. Notably, unlike the pattern presented in Fig. 16**a**, HS-ECC showed a lower carbon footprint than FA-based EGC because it is difficult to fully activate pure FA and gain high compressive strength for FA-based EGC. Here, it is worth mentioning that G1.0 and G1.5 still showed lower embodied carbon per SD Index (69.46 and 71.29 kg CO_2/m^3/MPa) compared to the referred cement-based HS-ECC, indicating the coupled greenness and high performance of the HS-EGC developed in this study.

5.3.2. Comparisons of embodied energy

Embodied energy indicates the nonrenewable energy consumed from material acquisition, processing, manufacturing, transportation, and construction throughout the whole life cycle. The embodied energy and embodied energy per SD Index of HS-EGC, FA-based EGC, and HS-ECC are presented in Fig. 17**a** and Fig. 17**b**, respectively. Generally, the comparison results of embodied energy showed similar trends with those of embodied carbon, where HS-EGC (3815.3–4505.4 MJ/m^3) and FA-based EGC (4204.0–6559.0 MJ/m^3) showed much lower embodied energy than the cement-based HS-ECC (around 6230.6–7339.4 MJ/m^3). In all the three groups of materials, PE and PVA fibers are the major sources of embodied carbon. Apart from this factor, the main contributor of embodied energy in HS-ECC was Portland cement, while those in HS-EGC and FA-based EGC were alkaline activators (sodium silicate and NaOH), which are similar to the embodied carbon results. Additionally, the increase of the silica modulus of alkaline activators resulted in higher embodied energy, which is also the same as the findings of embodied carbon analysis. In terms of embodied energy per SD Index (Fig. 17**b**), the developed HS-EGC (especially G1.0 and G1.5) showed the lowest energy consumption among the FA-based EGC groups, which further indicated the greenness of the HS-EGC developed in this study. Notably, G1.5 recorded the lowest embodied energy per SD Index (669.99 J/m^3/MPa) among all the compared mixes, although the mechanical performances of some mixes of HS-ECC were higher (e.g., the mix produced by Zhou et al. [102]).

5.3.3. Comparisons of material costs

The market potentials of construction materials are highly dependent on their material costs. Fig. 18**a** and Fig. 18**b** show the material cost and material cost per SD Index of HS-EGC, FA-based EGC and HS-ECC, respectively. As can be seen from the figure, the material costs also presented a similar trend to the results of embodied carbon and embodied energy. Obviously, clinker-free HS-EGC (4186.5–4230.7 CNY/m^3) and FA-based EGC had lower material costs (3505.5–4731.8 CNY/m^3) than cement-based HS-ECC (4734.7–5291.2 CNY/m^3).

It is mentioned that more than 60 % of the total material costs come from PE or PVA fibers, indicating that alternative fiber types of higher sustainability and cheaper price are desirable for strain-hardening geopolymer/cementitious materials. In the aspect of matrices, the matrix price of cement-based HS-ECC looks higher than that of FA-based EGC and HS-EGC. The material costs of EGC materials mainly come from FA, FSS, and alkaline activators, while those of HS-EGC mainly consist of cement, SF, SP, FSS, and possible supplementary cementitious materials such as FA and GGBS. This result indicated that almost all the components (except for water) would have an obvious impact on material costs of cementitious/geopolymer materials, and it is meaningful to look for diversified waste or cheaper raw materials to replace certain components in such construction materials. Generally, the material costs of HS-EGC developed in this study showed similar values with FA-based EGC from existing literature, while the cost efficiency of HS-EGC developed in this study was higher (due to higher mechanical performance). Furthermore, the increase of the silica modulus of alkaline activators slightly increased the material costs of HS-EGC. Regarding the material cost per SD Index, HS-EGC developed in this study (especially G1.0 and G1.5) obviously showed the lowest values among the FA-based EGC groups, benefiting from both comparatively cheap matrices and the high mechanical performances of this material. Especially, as the highest

Table 6
Mechanical properties and estimated embodied carbon, embodied energy, and material costs of FA-based EGC and HS-ECC with similar compressive strengths from existing literature.

Materials	Literature		Ref.	Curing Regime	Tensile Strain Capacity (%)	Compressive Strength (MPa)	Strength-Ductility (SD) Index (MPa)	Embodied Carbon (kg CO_2/m^3)	Embodied Energy (MJ/m^3)	Material Costs (CNY/m^3)	Embodied Carbon per SD Index (kg CO_2/m^3/MPa)	Embodied Energy per SD Index (MJ/m^3/MPa)	Material Costs per SD Index (CNY/m^3/MPa)
FA-based EGC	This Work	**G1.0**	/	90°C (72 h)	6.0	89.9	5.4	375.1	3815.3	4186.5	69.46	706.54	775.29
		G1.5	/		6.7	93.0	6.2	442.0	4153.9	4208.3	71.29	669.99	678.75
		G2.0	/		6.5	73.5	4.8	511.5	4505.4	4230.7	106.56	938.62	881.40
	(1)	Ohno and Li (2014)	[77]	60°C (8 h) + RT (28d)	4.3	27.6	1.2	306.9	4597.9	4176.6	255.7	3831.6	3480.5
	(2)	Nematollahi et al. (2015)	[78]	60°C (24 h) + RT (3d)	4.3	63.7	2.7	387.8	4870.5	3986.6	143.6	1803.9	1476.5
	(3)	Nematollahi et al. (2016)	[79]	60°C (24 h) + RT (3d)	4.3	63.7	2.7	387.8	4870.5	3986.6	143.6	1803.9	1476.5
	(4)	Nematollahi et al. (2017)	[80]	60°C (24 h) + RT (3d)	3.6	56.8	2.0	397.5	4876.2	4175.8	198.7	2438.1	2087.9
	(5)	Shaikh et al. (2018)	[81]	80°C (24 h) + RT (28d)	2.5	30.0	0.8	571.8	6141.9	4564.9	714.7	7677.4	5706.1
	(6)	Ohno and Li (2018)	[25]	60°C (24 h) + RT (28d)	4.4	43.3	1.9	289.2	4498.9	4276.2	152.2	2367.9	2250.6
	(7)	Ling et al. (2019)	[21]	50°C (24 h) + RT (28d)	3.1	73.3	2.3	206.8	4093.3	3943.3	89.9	1779.7	1714.5
	(8)	Farooq et al. (2019)	[100]	80°C (4 h) + RT (14d)	0.78	39.2	0.3	465.4	5994.6	4731.8	1551.2	19982.0	15772.6
	(9)	Farooq et al. (2020)	[82]	RT (72d)	2.0	23.7	0.5	539.0	6559.0	4603.4	1077.9	13118.0	9206.9
	(10)	Kan et al. (2020a)	[83]	80°C (2 h) + RT (28d)	4.0	18.9	0.8	312.6	4204.0	3586.0	390.7	5255.0	4482.5
	(11)	Kan et al. (2020b)	[84]	80°C (28d)	5.2	33.1	1.7	408.0	5477.2	3505.5	240.0	3211.9	2062.0
	(12)	Nguyễn et al. (2021)	[41]	RT (5d) + 80°C (1.5d) + RT (22.5d)	13.7	19.3	2.6	421.5	4812.3	3640.8	162.1	1850.9	1400.3
	(13)	Humur and Çevik (2022)	[85]	70°C (24 h) + RT (28d)	2.7	16.7	0.5	403.5	5143.0	4088.1	806.9	10286.0	8176.1
	(14)	Nguyễn et al. (2023)	[86]	RT (4d) + 120°C (12 h)	6.1	32.5	2.0	477.5	5443.4	4125.7	238.8	2721.7	2062.8
HS-ECC	(1)	Sui et al. (2018)	[101]	RT (28d)	6.7	102.8	6.9	783.3	6340.6	5155.0	113.5	918.9	747.1
	(2)	Zhou et al. (2018)	[102]	RT (28d)	9.0	99.5	9.0	810.6	6429.0	5291.2	90.1	714.3	587.9
	(3)	Lei et al. (2019)	[103]	85°C (9d) + RT (5d)	3.1	96.5	3.0	880.0	7339.4	4917.8	293.3	2446.5	1639.3
	(4)	Zhang et al. (2019)	[104]	RT (28d)	4.2	84.3	3.5	761.8	6230.6	4734.7	217.7	1780.2	1352.8
	(5)	Zhang et al. (2020)	[105]	RT (28d)	4.2	82.6	3.5	773.1	6299.6	4801.7	220.9	1799.9	1371.9

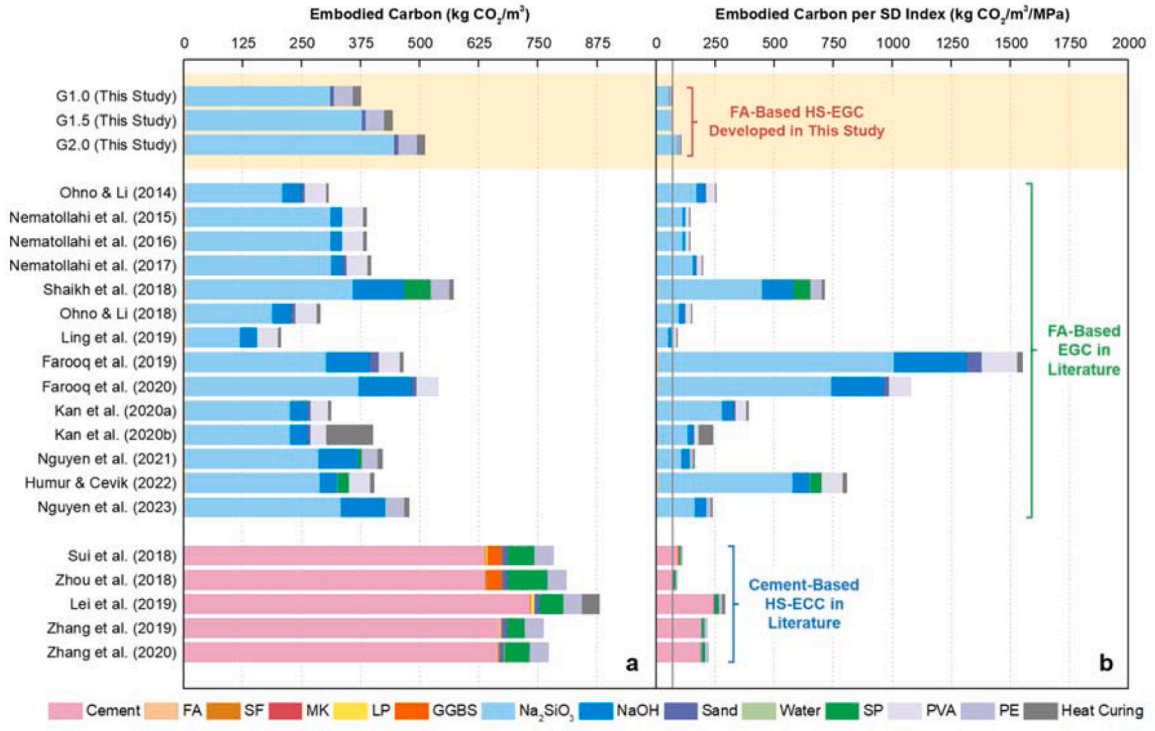

Fig. 16. Comparison of HS-EGC, FA-based EGC and HS-ECC with similar compressive strength: (a) Embodied carbon, and (b) embodied carbon per SD Index. The HS-EGC developed in this study (especially G1.0) showed the lowest embodied carbon per SD Index in the FA-based EGC family.

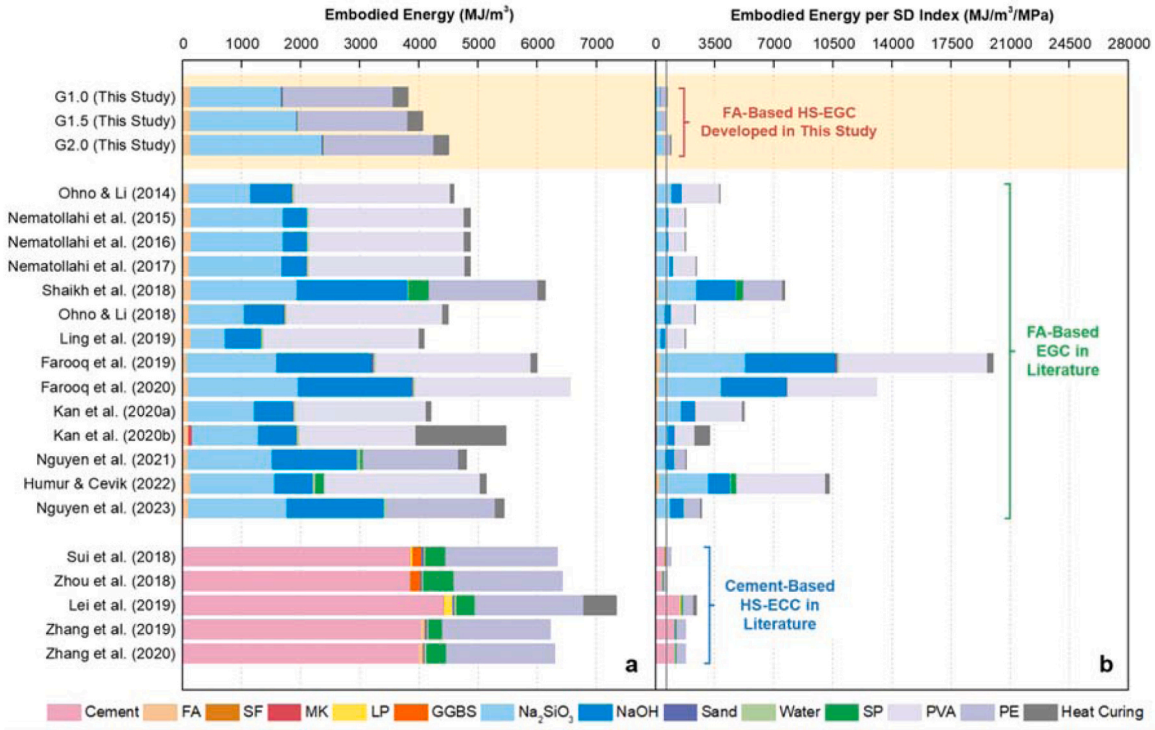

Fig. 17. Comparison of HS-EGC, FA-based EGC and HS-ECC with similar compressive strength: (a) Embodied energy, and (b) embodied energy per SD Index. G1.5 recorded the lowest embodied energy per SD Index among all the compared mixes.

compressive strength and tensile ductility was achieved in G1.5 in this study, the lowest material cost per SD Index was obtained in this mix (678.75 CNY/m^3/MPa) instead of G1.0 (775.29 CNY/m^3/MPa). However, it should also be mentioned that among all the referred mixes, the lowest material cost per SD Index was achieved in HS-ECC developed by Zhou et al. [102] (i.e., 587.9 CNY/m^3/MPa), due to its excellent mechanical performances.

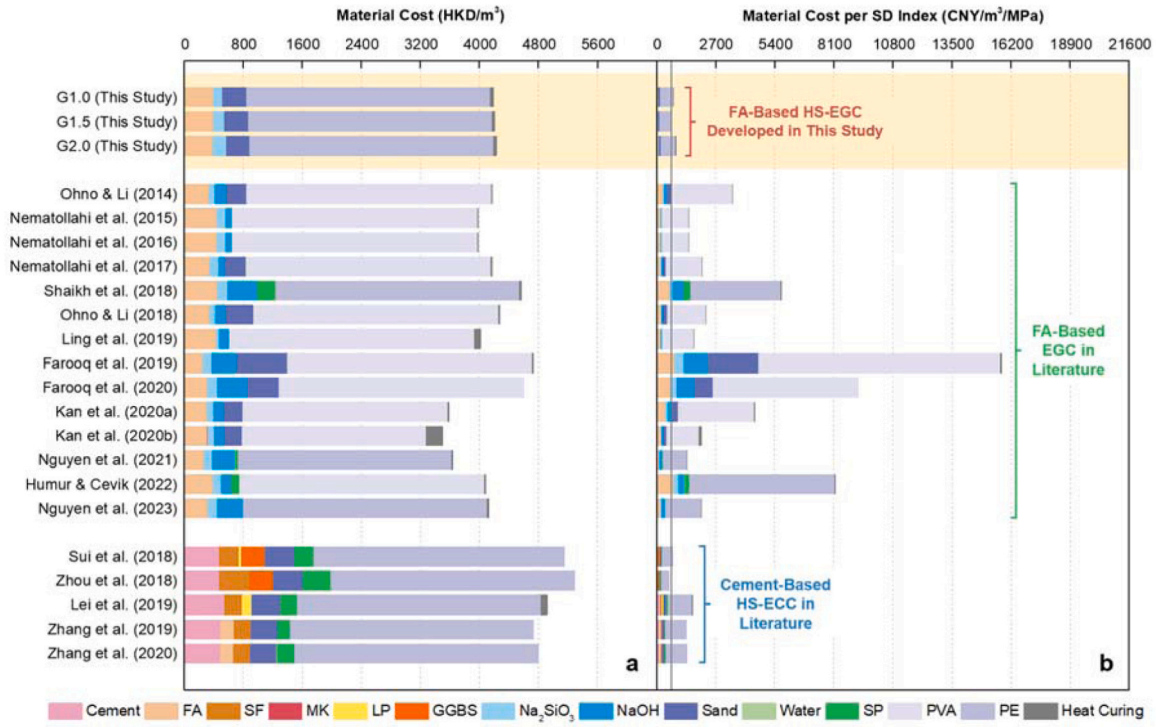

Fig. 18. Comparison of HS-EGC, FA-based EGC and HS-ECC with similar compressive strength: (a) Material cost, and (b) material cost per SD Index. For FA-based EGC, the lowest material cost per SD Index was obtained in G1.5.

6. Conclusions

In this study, a comprehensive experimental work was conducted to explore the influence of the silica modulus of alkaline activators on the tensile strain-hardening behavior and microstructures of pure fly ash (FA)-based High-Strength Engineered Geopolymer Composites (HS-EGC). Based on the analysis results, conclusions can be drawn as follows:

- EGC mixes with silica moduli of 1.0 and 1.5 showed compressive strengths over 80 MPa, which could be strictly classified as HS-EGC. The mixture with the silica modulus of 1.5 recorded the highest compressive strength (93.0 MPa), and the further increase of the silica modulus would hinder the geopolymerization and was not beneficial for the strength gain of FA-based HS-EGC.
- Distinguished strain-hardening behaviors were observed in all the HS-EGC mixes. The increase of silica modulus would cause a reduction in both tensile cracking strength and tensile strength of HS-EGC, as well as a resultant decreasing strain energy density. In terms of tensile strain capacity, the highest value was achieved in the mix with a silica modulus of 1.5 (6.7 %), and this mix also recorded the highest index of overall mechanical performances.
- Remarkable inflection points and double-stage patterns were observed in the tensile stress-strain curves, crack number evolution curves, and crack width evolution curves of all the HS-EGC mixes, owing to the over-saturated cracking phenomenon. At the first stage, the conventional steady-state multiple crack evolution dominated with a stable crack number increase but slow crack opening, while at the second stage (over-saturated cracking), crack number increased more slowly but the crack opening was distinguished.
- From BSE results, HS-EGC with the silica modulus of 1.5 showed the densest microstructures with the least unreacted FA particles, the mix with the silica modulus of 1.0 had a comparatively dense microstructure but still possessed a large amount of unreacted FA particles, while the mix with the silica modulus of 2.0 had the largest number of macro pores, which could explain the differed mechanical performances of the three mixes. EDS results also demonstrated the highest reaction degree of the HS-EGC mix with the silica modulus of 1.5.
- From the literature review of FA-based EGC and cement-based High-Strength Engineered Cementitious Materials (HS-ECC) with similar compressive strength, it was found that the embodied carbon, embodied energy, and materials costs of the developed HS-EGC were lower than those of the HS-ECC counterparts. Especially when coupled mechanical performances and sustainability indices were considered, the developed HS-EGC almost showed the best indices among all the currently available FA-based EGC and HS-ECC materials. The above finding indicated a sustainable feature and good market potential of the developed HS-EGC. Additionally, both high compressive strength (over 90 MPa) and high tensile strain capacity (over 6 %) were first achieved for pure FA-based EGC materials, which successfully pushed the performance envelope of this type of construction material.

Finally, although the influence of the silica modulus on the mechanical performances of HS-EGC was investigated in this study, limitations still exist in the experimental design and research scope. For example, the gradient settings of silica modulus (i.e., 1.0, 1.5 and 2.0) were limited, and more variables (e.g., 1.25 and 1.75) are suggested to be investigated in the future. Furthermore, the influence of the silica modulus of alkaline activators on the durability (e.g., chloride resistance, sulfate resistance, and long-term drying shrinkage) should also be paid attention to in the further studies. Efforts on utilizing waste-derived alkali [106] and alternative activators (e.g., Na_2CO_3 [107]) with better sustainability are also appreciated to further improve the greenness and cost efficiency of pure fly ash-based HS-EGC materials.

CRediT authorship contribution statement

Ling-Yu Xu: Writing – original draft, Validation, Investigation, Formal analysis, Conceptualization. **Jian-Cong Lao:** Writing – review & editing, Investigation, Data curation. **Lan-Ping Qian:** Writing – review & editing, Visualization, Validation, Methodology, Formal analysis.

Mehran Khan: Writing – review & editing, Formal analysis. **Tian-Yu Xie:** Writing – review & editing, Supervision. **Bo-Tao Huang:** Writing – review & editing, Visualization, Supervision, Investigation, Funding acquisition, Conceptualization.

Declaration of Competing Interest

The authors declare that they have no known competing financial interests or personal relationships that could have appeared to influence the work reported in this paper.

Data availability

Data will be made available on request.

Acknowledgments

The authors would like to acknowledge the support of the National Natural Science Foundation of China (No. 52308290 and 52409179), China Postdoctoral Science Foundation (No. 2024M752800), the National Natural Science Fund for Excellent Young Scientists Fund Program (Overseas), and the Science and Technology Program Project of the Department of Communication of Zhejiang Province (No. 2024001).

References

[1] V.C. Li, Engineered Cementitious Composites (ECC) - Bendable Concrete for Sustainable and Resilient Infrastructure. Verlag GmbH Germany, Springer, Berlin, Heidelberg, 2019.
[2] L.Y. Xu, B.T. Huang, V.C. Li, J.G. Dai, High-strength high-ductility Engineered/Strain-Hardening Cementitious Composites (ECC/SHCC) incorporating geopolymer fine aggregates, Cem. Concr. Compos. 125 (2022) 104296.
[3] J. Cai, J. Pan, X. Li, Behavior of ECC-encased CFST columns under axial compression, Eng. Struct. 171 (2018) 1–9.
[4] R. Zhong, F. Zhang, L.H. Poh, S. Wang, H.T.N. Le, M.H. Zhang, Assessing the Effectiveness of UHPFRC, FRHSC and ECC Against High Velocity Projectile Impact, Cem. Concr. Compos. 120 (2021) 104013.
[5] J. Li, W. Dong, X. Zhao, H. Li, Investigation on fracture properties of concrete considering the viscoelastic characteristics, Constr. Build. Mater. 426 (2024) 136044.
[6] X. Zhu, H. Abe, D. Hayashi, H. Tanaka, Behavioral characteristics of RC beams with non-uniform corrosion along the reinforcement, J. Intell. Constr. 1 (3) (2023) 9180019.
[7] H. Su, X. Xu, S. Zuo, S. Zhang, X. Yan, Research progress in monitoring hydraulic concrete damage based on acoustic emission, J. Intell. Constr. 1 (4) (2023) 9180024.
[8] G. Yao, W. Sun, Y. Yang, M. Wang, R. Li, Y. Zheng, Multi-volume variable scale bitmap data object classification algorithm architectural concrete color difference detection, J. Intell. Constr. 1 (2) (2023) 1–17.
[9] R. Zhong, K. Wille, Deterioration of residential concrete foundations: the role of pyrrhotite-bearing aggregate, Cem. Concr. Compos. 94 (2018) 53–61.
[10] R. Zhong, F.L. Zhang, Engineering high performance cementitious matrix for improved projectile impact resistance with silane, micro fibrillated cellulose and fine calcined bauxite aggregate, Cem. Concr. Compos. 135 (2023) 104835.
[11] Z. Jiang, Z. Ge, T. Wang, H. Gao, Y. Zhang, B. Ling, Šavija, Size effect on compressive strength of foamed concrete: experimental and numerical studies, Mater. Des. 240 (2024) 112841.
[12] D. Lu, X. Jiang, Y. Zhang, S. Zhang, G. Lu, Z. Leng, A state-of-the-art review of the development of self-healing concrete for resilient infrastructure, Front. Struct. Civ. Eng. (2024) 1–19.
[13] X. Jiang, H. Zhu, Z. Yan, F. Zhang, X. Huang, Z. Leng, R. Xiao, Fire-retarding asphalt pavement for urban road tunnels: a state-of-the-art review and beyond, Fire Technol. (2024) 1–41.
[14] X. Jiang, F. Zhang, B. Huang, H. Titi, P. Polaczyk, Y. Ma, Z. Cheng, Full-scale accelerated testing of geogrid-reinforced inverted pavements, Geotext. Geomembr. 52 (4) (2024) 511–525.
[15] X. Jiang, D. Lu, B. Yin, Z. Leng, Advancing carbon nanomaterials-engineered self-sensing cement composites for structural health monitoring: a state-of-the-art review, J. Build. Eng. (2024) 109129.
[16] X. Jiang, R. Xiao, Y. Bai, B. Huang, Y. Ma, Influence of waste glass powder as a supplementary cementitious material (SCM) on physical and mechanical properties of cement paste under high temperatures, J. Clean. Prod. 340 (2022) 130778.
[17] B.T. Huang, K.F. Weng, J.X. Zhu, Y. Xiang, J.G. Dai, V.C. Li, Engineered/strain-hardening cementitious composites (ECC/SHCC) with an ultra-high compressive strength over 210 MPa, Compos. Commun. 26 (2021) 100775.
[18] J.X. Zhu, L.Y. Xu, B.T. Huang, K.F. Weng, J.G. Dai, Recent developments in engineered/strain-hardening cementitious composites (ECC/SHCC) with high and ultra-high strength, Constr. Build. Mater. 342 (2022) 127956.
[19] L.Y. Xu, B.T. Huang, Q. Lan-Ping, J.G. Dai, Enhancing long-term tensile performance of engineered cementitious composites (ECC) using sustainable artificial geopolymer aggregates, Cem. Concr. Compos. 133 (2022) 104676.
[20] H. Zhong, M. Zhang, Engineered geopolymer composites: a state-of-the-art review, Cem. Concr. Compos. (2022) 104850.
[21] Y. Ling, K. Wang, W. Li, G. Shi, P. Lu, Effect of slag on the mechanical properties and bond strength of fly ash-based engineered geopolymer composites, Compos. Part B: Eng. 164 (2019) 747–757.
[22] J. Jia, W.A. Baah, C. Zheng, L. Ding, Y. Wu, New stress–strain model and intelligent quality control technology for cemented material dam, J. Intell. Constr. 2 (1) (2024) 9180033.
[23] I. Cavusoglu, E. Yilmaz, A.O. Yilmaz, Additivity effect on properties of cemented coal fly ash backfill containing water-reducing admixtures, Constr. Build. Mater. 267 (2021) 121021.
[24] J. Li, S. Cao, E. Yilmaz, Characterization of macro mechanical properties and microstructures of cement-based composites prepared from fly ash, gypsum and steel slag, Minerals 12 (1) (2021) 6.
[25] M. Ohno, V.C. Li, An integrated design method of engineered geopolymer composite, Cem. Concr. Compos. 88 (2018) 73–85.
[26] L.Y. Xu, Y. Alrefaei, Y.S. Wang, J.G. Dai, Recent advances in molecular dynamics simulation of the NASH geopolymer system: modeling, structural analysis, and dynamics, Constr. Build. Mater. 276 (2021) 122196.
[27] L.Y. Xu, L.P. Qian, B.T. Huang, J.G. Dai, Development of artificial one-part geopolymer lightweight aggregates by crushing technique, J. Clean. Prod. 315 (2021) 128200.
[28] L.P. Qian, B.T. Huang, L.Y. Xu, J.G. Dai, Concrete made with high-strength artificial geopolymer aggregates: mechanical properties and failure mechanisms, Constr. Build. Mater. 367 (2023) 130318.
[29] L.P. Qian, L.Y. Xu, B.T. Huang, J.G. Dai, Pelletization and properties of artificial lightweight geopolymer aggregates (GPA): One-part vs. two-part geopolymer techniques, J. Clean. Prod. 374 (2022) 133933.
[30] T. Cakmak, I. Ustabas, Z. Kurt, E. Yilmaz, Geopolymer mortars having glassy materials considering mechanical and microstructural features, J. Build. Eng. 91 (2024) 109738.
[31] J. Cai, X. Li, J. Tan, B. Vandevyvere, Thermal and compressive behaviors of fly ash and metakaolin-based geopolymer, J. Build. Eng. 30 (2020) 101307.
[32] J. Cai, X. Li, J. Tan, B. Vandevyvere, Fly ash-based geopolymer with self-heating capacity for accelerated curing, J. Clean. Prod. 261 (2020) 121119.
[33] J. Cai, J. Tan, X. Li, Thermoelectric behaviors of fly ash and metakaolin based geopolymer, Constr. Build. Mater. 237 (2020) 117757.
[34] X. Jiang, H. Zhu, Z. Yan, F. Zhang, F. Ye, P. Li, B. Huang, A state-of-art review on development and progress of backfill grouting materials for shield tunneling, Dev. Built Environ. (2023) 100250.
[35] Z.F. Akbulut, S. Guler, M. Khan, The effects of waste iron powder and steel fiber on the physical and mechanical properties of geopolymer mortars exposed to high temperatures (December), in: Structures, Vol. 58, Elsevier, 2023 105398 (December).
[36] N. Zhang, C. Yan, L. Li, M. Khan, Assessment of fiber factor for the fracture toughness of polyethylene fiber reinforced geopolymer, Constr. Build. Mater. 319 (2022) 126130.
[37] J. Cai, J. Pan, J. Han, Y. Lin, Z. Sheng, Impact behaviours of engineered geopolymer composite exposed to elevated temperatures, Constr. Build. Mater. 312 (2021) 125421.
[38] J. Cai, J. Pan, J. Han, Y. Lin, Z. Sheng, Low-energy impact behavior of ambient cured engineered geopolymer composites, Ceram. Int. 48 (7) (2022) 9378–9389.
[39] J. Han, J. Cai, Y. Lin, Y. Sun, J. Pan, Impact resistance of engineered geopolymer composite (EGC) in cold temperatures, Constr. Build. Mater. 343 (2022) 128150.
[40] J.C. Lao, B.T. Huang, L.Y. Xu, M. Khan, Y. Fang, J.G. Dai, Seawater sea-sand Engineered Geopolymer Composites (EGC) with high strength and high ductility, Cem. Concr. Compos. 138 (2023) 104998.
[41] H.H. Nguyễn, Q.H. Lương, J.I. Choi, R. Ranade, V.C. Li, B.Y. Lee, Ultra-ductile behavior of fly ash-based engineered geopolymer composites with a tensile strain capacity up to 13.7%, Cem. Concr. Compos. 122 (2021) 104133.
[42] Q.H. Lương, H.H. Nguyễn, P.H. Nguyễn, S.T. Kang, B.Y. Lee, Extremely-ductile alkali-activated slag-based composite with a tensile strain capacity up to 22%, Ceram. Int. 49 (8) (2023) 12069–12078.
[43] J.C. Lao, B.T. Huang, Y. Fang, L.Y. Xu, J.G. Dai, S.P. Shah, Strain-hardening alkali-activated fly ash/slag composites with ultra-high compressive strength and ultra-high tensile ductility, Cem. Concr. Res. 165 (2023) 107075.
[44] X. Gao, Q.L. Yu, H.J.H. Brouwers, Reaction kinetics, gel character and strength of ambient temperature cured alkali activated slag–fly ash blends. Constr. Build. Mater. 80 (2015) 105–115.
[45] N. Hammad, A. El-Nemr, H.E.D. Hasan, The performance of fiber GGBS based alkali-activated concrete, J. Build. Eng. 42 (2021) 102464.
[46] J.C. Lao, R.Y. Ma, L.Y. Xu, Y. Li, Y.N. Shen, J. Yao, B.T. Huang, Fly ash-dominated high-strength engineered/strain-hardening geopolymer composites (HS-EGC/SHGC): influence of alkalinity and environmental assessment, J. Clean. Prod. 447 (2024) 141182.
[47] H. Pan, Z. Xie, G. Chen, J. Su, K. Zhuo, Z. Chen, Y. Guo, Dynamic compressive behavior of high-strength engineered geopolymer composites, J. Build. Eng. 80 (2023) 108036.
[48] N.K. Lee, J.G. Jang, H.K. Lee, Shrinkage characteristics of alkali-activated fly ash/slag paste and mortar at early ages, Cem. Concr. Compos. 53 (2014) 239–248.

[49] S.M. Park, J.G. Jang, N.K. Lee, H.K. Lee, Physicochemical properties of binder gel in alkali-activated fly ash/slag exposed to high temperatures, Cem. Concr. Res. 89 (2016) 72–79.
[50] J. Xie, J. Wang, R. Rao, C. Wang, C. Fang, Effects of combined usage of GGBS and fly ash on workability and mechanical properties of alkali activated geopolymer concrete with recycled aggregate, Compos. Part B: Eng. 164 (2019) 179–190.
[51] M. Sivasakthi, R. Jeyalakshmi, Effect of change in the silica modulus of sodium silicate solution on the microstructure of fly ash geopolymers, J. Build. Eng. 44 (2021) 102939.
[52] Chinese Standard GB/T 14684-2011, Sand for Construction, Standardization Administration of People's Republic of China, Beijing, China, 2011 (In Chinese).
[53] ASTM C1437, Standard Test Method for Flow of Hydraulic Cement Mortar, ASTM International, West Conshohocken, PA, 2020.
[54] ASTM C109/C109M, Standard Test Method for Compressive Strength of Hydraulic Cement Mortars, ASTM International, West Conshohocken, PA, 2013.
[55] Japan Society of Civil Engineers, Recommendations for Design and Construction of High Performance Fiber Reinforced Cement Composites with Multiple Fine Cracks (HPFRCC), Concrete Engineering Series No, 2008, p. 82.
[56] Y. Yang, X. Gao, H. Deng, P. Yu, Y. Yao, Effects of water/binder ratio on the properties of engineered cementitious composites, J. Wuhan. Univ. Technol. -Mater. Sci. Ed. 25 (2) (2010) 298–302.
[57] Y. Yang, Y. Yao, X. Gao, H. Deng, P. Yu, Shrinkage reducing measures for engineering cementitious composites, J. Wuhan. Univ. Technol. -Mater. Sci. Ed. 23 (6) (2008) 907–911.
[58] S. Zhang, V.C. Li, G. Ye, Micromechanics-guided development of a slag/fly ash-based strain-hardening geopolymer composite, Cem. Concr. Compos. 109 (2020) 103510.
[59] L.Y. Xu, B.T. Huang, J.C. Lao, J. Yao, V.C. Li, J.G. Dai, Tensile over-saturated cracking of Ultra-High-Strength Engineered Cementitious Composites (UHS-ECC) with artificial geopolymer aggregates, Cem. Concr. Compos. 136 (2023) 104896.
[60] P. Li, H. Wang, D. Nie, D. Wang, C. Wang, A method to analyze the long-term durability performance of underground reinforced concrete culvert structures under coupled mechanical and environmental loads, J. Intell. Constr. 1 (2) (2023) 9180011.
[61] X. Sun, S. Wang, J. Jin, Z. Wang, F. Gong, Computational methods of mass transport in concrete under stress and crack conditions: a review, J. Intell. Constr. 1 (2) (2023) 9180015.
[62] Z. Wang, F. Gong, K. Maekawa, Multi-scale and multi-chemo–physics lifecycle evaluation of structural concrete under environmental and mechanical impacts. J. Intell. Constr. 1 (1) (2023) 9180003.
[63] F. Gong, X. Sun, Y. Takahashi, K. Maekawa, W. Jin, Computational modeling of combined frost damage and alkali–silica reaction on the durability and fatigue life of RC bridge decks, J. Intell. Constr. 1 (1) (2023) 9180001.
[64] R. Zhong, X. Ai, M. Pan, Y. Yao, Z. Cheng, X. Peng, J. Wang, W. Zhou, Durability of Micro-Cracked UHPC Subjected to Coupled Freeze-Thaw and Chloride Salt Attacks, Cem. Concr. Compos. 148 (2024) 105471.
[65] M. Xu, S. Song, L. Feng, J. Zhou, H. Li, V.C. Li, Development of basalt fiber engineered cementitious composites and its mechanical properties, Constr. Build. Mater. 266 (2021) 121173.
[66] V.C. Li, On engineered cementitious composites (ECC) a review of the material and its applications, J. Adv. Concr. Technol. 1 (3) (2003) 215–230.
[67] T. Kanda, V.C. Li, Multiple cracking sequence and saturation in fiber reinforced cementitious composites, Concr. Res. Technol. 9 (2) (1998) 457–468.
[68] X. Ouyang, Y. Ma, Z. Liu, J. Liang, G. Ye, Effect of the sodium silicate modulus and slag content on fresh and hardened properties of alkali-activated fly ash/slag, Minerals 10 (1) (2019) 15.
[69] P. Duxson, J.L. Provis, G.C. Lukey, S.W. Mallicoat, W.M. Kriven, J.S. Van Deventer, Understanding the relationship between geopolymer composition, microstructure and mechanical properties, Colloids Surf. A: Physicochem. Eng. Asp. 269 (1-3) (2005) 47–58.
[70] J.J. Chang, A study on the setting characteristics of sodium silicate-activated slag pastes, Cem. Concr. Res. 33 (7) (2003) 1005–1011.
[71] Sindhunata, J.S.J. Van Deventer, G.C. Lukey, H. Xu, Effect of curing temperature and silicate concentration on fly-ash-based geopolymerization, Ind. Eng. Chem. Res. 45 (10) (2006) 3559–3568.
[72] A.S. De Vargas, D.C. Dal Molin, A.C. Vilela, F.J. Da Silva, B. Pavao, H. Veit, The effects of Na2O/SiO2 molar ratio, curing temperature and age on compressive strength, morphology and microstructure of alkali-activated fly ash-based geopolymers, Cem. Concr. Compos. 33 (6) (2011) 653–660.
[73] X. Gao, A. Zhang, S. Li, B. Sun, L. Zhang, The resistance to high temperature of magnesia phosphate cement paste containing wollastonite, Mater. Struct. 49 (2016) 3423–3434.
[74] B. Sun, Q. Zeng, D. Wang, W. Zhao, Sustainable 3D printed mortar with CO2 pretreated recycled fine aggregates, Cem. Concr. Compos. 134 (2022) 104800.
[75] J. Davidovits, Geopolymers: man-made rock geosynthesis and the resulting development of very early high strength cement, J. Mater. Educ. 16 (1994), 91-91.
[76] B.T. Huang, J.X. Zhu, K.F. Weng, V.C. Li, J.G. Dai, Ultra-high-strength engineered/strain-hardening cementitious composites (ECC/SHCC): Material design and effect of fiber hybridization, Cem. Concr. Compos. 129 (2022) 104464.
[77] M. Ohno, V.C. Li, A feasibility study of strain hardening fiber reinforced fly ash-based geopolymer composites, Constr. Build. Mater. 57 (2014) 163–168.
[78] B. Nematollahi, J. Sanjayan, F.U. Ahmed Shaikh, Tensile strain hardening behavior of PVA fiber-reinforced engineered geopolymer composite, J. Mater. Civ. Eng. 27 (10) (2015) 04015001.
[79] B. Nematollahi, J. Sanjayan, F.U.A. Shaikh, Matrix design of strain hardening fiber reinforced engineered geopolymer composite, Compos. Part B: Eng. 89 (2016) 253–265.
[80] B. Nematollahi, J. Qiu, E.H. Yang, J. Sanjayan, Microscale investigation of fiber-matrix interface properties of strain-hardening geopolymer composite, Ceram. Int. 43 (17) (2017) 15616–15625.
[81] F.U.A. Shaikh, A. Fairchild, R. Zammar, Comparative strain and deflection hardening behaviour of polyethylene fibre reinforced ambient air and heat cured geopolymer composites, Constr. Build. Mater. 163 (2018) 890–900.
[82] M. Farooq, A. Bhutta, N. Banthia, Strain-hardening ambient-cured eco-friendly ductile geopolymer composites, Acids Mater. J. 117 (3) (2020) 181–189.
[83] L. Kan, L. Zhang, Y. Zhao, M. Wu, Properties of polyvinyl alcohol fiber reinforced fly ash based Engineered Geopolymer Composites with zeolite replacement, Constr. Build. Mater. 231 (2020) 117161.
[84] L.L. Kan, W.S. Wang, W.D. Liu, M. Wu, Development and characterization of fly ash based PVA fiber reinforced Engineered Geopolymer Composites incorporating metakaolin, Cem. Concr. Compos. 108 (2020) 103521.
[85] G. Humur, A. Çevik, Mechanical characterization of lightweight engineered geopolymer composites exposed to elevated temperatures, Ceram. Int. 48 (10) (2022) 13634–13650.
[86] P.H. Nguyễn, H.H. Nguyễn, Q.H. Lương, J.E. Bolander, B.Y. Lee, Optimization of fly ash-based polyethylene fiber-reinforced engineered cement-free composites with low-density and ultra-ductility using Taguchi robust design method, J. Build. Eng. 66 (2023) 105946.
[87] V. Shobeiri, B. Bennett, T. Xie, P. Visintin, A comprehensive assessment of the global warming potential of geopolymer concrete, J. Clean. Prod. 297 (2021) 126669.
[88] Y. Fang, M.R. Ahmad, J.C. Lao, L.P. Qian, J.G. Dai, Development of artificial geopolymer aggregates with thermal energy storage capacity, Cem. Concr. Compos. 135 (2023) 104834.
[89] S. Zhang, Z. Li, B. Ghiassi, S. Yin, G. Ye, Fracture properties and microstructure formation of hardened alkali-activated slag/fly ash pastes, Cem. Concr. Res. 144 (2021) 106447.
[90] J. Yu, Y. Chen, C.K. Leung, Mechanical performance of Strain-Hardening Cementitious Composites (SHCC) with hybrid polyvinyl alcohol and steel fibers, Compos. Struct. 226 (2019) 111198.
[91] T. Yang, Z. Zhang, F. Zhang, Y. Gao, Q. Wu, Chloride and heavy metal binding capacities of hydrotalcite-like phases formed in greener one-part sodium carbonate-activated slag cements, J. Clean. Prod. 253 (2020) 120047.
[92] L. Thannimalay, S. Yusoff, N.Z. Zawawi, Life cycle assessment of sodium hydroxide, Aust. J. Basic Appl. Sci. 7 (2) (2013) 421–431.
[93] L.N. Assi, K. Carter, E. Deaver, P. Ziehl, Review of availability of source materials for geopolymer/sustainable concrete, J. Clean. Prod. 263 (2020) 121477.
[94] M. Abdellatief, S.M. AL-Tam, W.E. Elemam, H. Alanazi, G.M. Elgendy, A. M. Tahwia, Development of ultra-high-performance concrete with low environmental impact integrated with metakaolin and industrial wastes, Case Stud. Constr. Mater. 18 (2023) e01724.
[95] P.P. Li, H.J.H. Brouwers, W. Chen, Q. Yu, Optimization and characterization of high-volume limestone powder in sustainable ultra-high performance concrete, Constr. Build. Mater. 242 (2020) 118112.
[96] G. Long, Y. Gao, Y. Xie, Designing more sustainable and greener self-compacting concrete, Constr. Build. Mater. 84 (2015) 301–306.
[97] J. Yu, H.L. Wu, C.K. Leung, Feasibility of using ultrahigh-volume limestone-calcined clay blend to develop sustainable medium-strength Engineered Cementitious Composites (ECC), J. Clean. Prod. 262 (2020) 121343.
[98] N. Vijayarethinam, Silica fume applications, World Cem. 40 (2009) 97–100.
[99] J. Yu, J. Yao, X. Lin, H. Li, J.Y. Lam, C.K. Leung, K. Shih, Tensile performance of sustainable Strain-Hardening Cementitious Composites with hybrid PVA and recycled PET fibers, Cem. Concr. Res. 107 (2018) 110–123.
[100] M. Farooq, A. Bhutta, N. Banthia, Tensile performance of eco-friendly ductile geopolymer composites (EDGC) incorporating different micro-fibers, Cem. Concr. Compos. 103 (2019) 183–192.
[101] L. Sui, Q. Zhong, K. Yu, F. Xing, P. Li, Y. Zhou, Flexural fatigue properties of ultra-high performance engineered cementitious composites (UHP-ECC) reinforced by polymer fibers, Polymers 10 (8) (2018) 892.
[102] Y. Zhou, B. Xi, K. Yu, L. Sui, F. Xing, Mechanical properties of hybrid ultra-high performance engineered cementitous composites incorporating steel and polyethylene fibers, Materials 11 (8) (2018) 1448.
[103] D.Y. Lei, L.P. Guo, B. Chen, I. Curosu, V. Mechtcherine, The connection between microscopic and macroscopic properties of ultra-high strength and ultra-high ductility cementitious composites (UHS-UHDCC), Compos. Part B: Eng. 164 (2019) 144–157.
[104] Z. Zhang, A. Yuvaraj, J. Di, S. Qian, Matrix design of light weight, high strength, high ductility ECC, Constr. Build. Mater. 210 (2019) 188–197.
[105] Z. Zhang, F. Yang, J.C. Liu, S. Wang, Eco-friendly high strength, high ductility engineered cementitious composites (ECC) with substitution of fly ash by rice husk ash, Cem. Concr. Res. 137 (2020) 106200.
[106] M.F. Alnahhal, T. Kim, A. Hajimohammadi, Waste-derived activators for alkali-activated materials: A review, Cem. Concr. Compos. 118 (2021) 103980.
[107] J.C. Lao, L.Y. Xu, B.T. Huang, J.X. Zhu, M. Khan, J.G. Dai, Utilization of sodium carbonate activator in strain-hardening ultra-high-performance geopolymer concrete (SH-UHPGC), Front. Mater. 10 (2023) 1142237.